Draft version November 5, 2015
Preprint typeset using LaTeX style emulateapj v. 12/16/11

A COUPLED 2×2D BABCOCK–LEIGHTON SOLAR DYNAMO MODEL. II. REFERENCE DYNAMO SOLUTIONS

Alexandre Lemerle[1,2] and Paul Charbonneau[1]

Draft version November 5, 2015

ABSTRACT

[The need for reliable predictions of the solar activity cycle continues to drive the development of dynamo models incorporating a representation of surface processes sufficiently detailed to allow assimilation of magnetographic data. In this series of paper we present one such dynamo model, and document its behavior and properties.] In this paper we complete the presentation of a new hybrid 2×2D flux transport dynamo model of the solar cycle based on the Babcock–Leighton mechanism of poloidal magnetic field regeneration via the surface decay of bipolar magnetic regions (BMR). This hybrid model is constructed by coupling the surface magnetic flux transport described in Lemerle et al. (2015) to an axisymmetric kinematic flux transport dynamo model defined in a meridional plane. The surface model provides the poloidal source term for the internal dynamo model via its outer boundary condition, while the latter generates the bipolar emergences which drive reversal of the surface dipole in the surface model. A key aspect of the coupled model is the definition of an emergence function describing the probability of BMR emergence as a function of the spatial distribution of internal axisymmetric magnetic field. We use a genetic algorithm (GA) to calibrate this function, together with other model parameters, against observed cycle 21 emergence data. Using these GA-calibrated best-fit parameter values, we present a reference dynamo solution reproducing many solar cycle characteristics, including good hemispheric coupling, phase relationship between the surface dipole and the BMR-generating internal field, correlation between dipole strength at cycle maximum and peak amplitude of the next cycle, and lack thereof between peak cycle amplitude and dipole strength of next minimum. The saturation of the mean cycle amplitude takes place only through the quenching of the mean BMR tilt as a function of erupting magnetic flux, as suggested by observational analyses. The observed statistical scatter about the mean BMR tilt, built into the model, acts as a strong source of stochasticity which dominates amplitude fluctuations, at least in the parameter regimes investigated so far. The model thus can produce Dalton-like epochs of strongly suppressed cycle amplitude lasting a few cycles. Although significant spectral power is produced at low frequencies, no Gleissberg-like long periodicities are apparent in the power spectra of magnetic energy, dipole moment, or other cycle characteristics. The dynamo can also shut off entirely following an unfavorable sequence of emergence events, usually through occasional emergence of a large BMR deviating significantly from Joy's law. Because it includes a spatially resolved representation of the solar photosphere, this hybrid model is particularly well-suited for providing synthetic data for coronal magnetic field reconstructions, as well as for assimilation of magnetographic data towards solar cycle forecasting.

Keywords: *Alex:* [A verifier] dynamo — Sun: activity — Sun: interior — Sun: magnetic fields — Sun: photosphere — sunspots

1. INTRODUCTION

Close to a century has now gone by since the discovery of the underlying magnetic nature of the eleven-year sunspot cycle (Hale et al. 1919). The magnetic polarity reversals of the leading and following (with respect to rotation) components of large bipolar magnetic regions (BMRs) is now thought to reflect the presence, somewhere in the solar interior, of a large-scale, dominantly axisymmetric zonally-oriented (toroidal) magnetic field, antisymmetric about the sun's equator and itself undergoing polarity reversals approximately every eleven years, for a full magnetic cycle period of $\simeq 22$ years. The rotational shear of a pre-existing dipole, later detected on the solar surface (Babcock & Babcock 1955), can act as an inductive source for such an internal toroidal magnetic flux system. However, closing the dynamo loop requires an inductive mechanism capable of regenerating the dipole from this internal toroidal component, in a manner such as leading the cyclic polarity reversals of both of these large-scale components of the solar magnetic field.

Many candidates for this toroidal-to-poloidal hydromagnetic inductive mechanisms have been identified, starting with cyclonic convection (Parker 1955) and its associated mean electromotive force, and the surface decay of bipolar magnetic regions (Babcock 1961), now referred to as the Babcock–Leighton (BL) mechanism. These were joined more recently by helical waves along thin magnetic flux tubes (Schmitt 1987; Ossendrijver 2000, and references therein), and shear instabilities in the tachocline (Dikpati & Gilman 2001), the stably stratified rotational shear layer located beneath the base of the solar convection zone, as revealed by helioseismol-

[1] Département de physique, Université de Montréal, 2900 boul. Édouard-Montpetit, Montréal, QC, H3T 1J4, Canada; lemerle@astro.umontreal.ca, paulchar@astro.umontreal.ca
[2] Collège de Bois-de-Boulogne, 10555 av. Bois-de-Boulogne, Montréal, QC, H4N 1L4, Canada.

ogy. In all cases, the rotational influence mediated by the Coriolis force is the key agent that breaks the mirror symmetry of the inductive flows, thus allowing to circumvent Cowling's theorem.

Of these various candidates for poloidal field regeneration, the BL mechanism stands out as the only one that can be directly observed operating at the solar surface, and as such is far better constrained than any other. In particular, the distribution of tilt angles of BMRs, namely the angle defined by a line segment joining each pole of the BMR measured with respect to the east–west direction, is now well characterized from white light (Howard 1991; Dasi-Espuig et al. 2010) and magnetographic observations (Wang & Sheeley 1989). This tilt arises through the action of the Coriolis force on the flows developing along the axis of buoyantly rising toroidal magnetic flux ropes, believed to be generated near the base of the solar convection zone, and eventually piercing the photosphere in the form of BMRs (see Fan 2009 for a review). Associated with this tilt is a net dipole moment so that, effectively, a poloidal magnetic component is being produced from a pre-existing toroidal component. The magnitude of this tilt, and its pattern of variations with latitude, BMR flux and separation, and statistical fluctuations about the mean, all play a key role in setting the magnitude of the surface dipole moment produced in the course of a sunspot cycle.

Because the BL mechanism operates at the solar surface, a transport mechanism is also needed to carry the surface poloidal magnetic field down into the interior, where rotational shearing is taking place. Here again a number of appropriate candidate mechanisms are available, including advection by large-scale meridional flows pervading the solar convection zone, as well as turbulent transport effects, namely isotropic diffusive transport and directional turbulent pumping. Viewed globally, the BL mechanism is a non-local inductive effect: the surface source of poloidal field is driven by the deep-seated toroidal component, on timescales much shorter than the magnetic cycle period.

Dynamo models of the solar cycle relying on the BL mechanism of poloidal field regeneration have undergone a vigorous revival in the last 25 years of so, spurred by Wang et al. (1989), Wang & Sheeley (1991), Choudhuri et al. (1995), and Durney (1995). Many such model are now dispersed in the literature (for recent reviews see Charbonneau 2010; Karak et al. 2014). The vast majority rely on a two-dimensional axisymmetric formulation of the problem, whereby the large-scale flows and magnetic field components are both axisymmetric, and the dynamo equations solved in a meridional (r, θ) plane. Typically, helioseismology-compatible parameterizations for solar-like internal differential rotation and meridional circulation are introduced, and these flows are assumed steady (the so-called kinematic approximation).

Many such models do differ in how they incorporate the BL mechanism, a fundamentally non-axisymmetric effect, into the axisymmetric dynamo equations (compare, e.g., Durney 1995; Dikpati & Charbonneau 1999; Nandy & Choudhuri 2001; Muñoz-Jaramillo et al. 2010). They also differ in assumptions made regarding the primary magnetic field transport mechanism. As a consequence, models based on rather different input physics can do roughly as well as one another in reproducing the primary characteristics of the observed solar cycle. However, the differences can matter a lot in practice. Perhaps no better illustration of this point can be found than the widely differing dynamo model-based predictions of sunspot cycle 24 made by Dikpati et al. (2006) and Choudhuri et al. (2007), each using a BL model "calibrated" to earlier sunspot cycles.

This problem is compounded when introducing data assimilation into the model-based prediction, as the datasets must then also be preprocessed in some way to accommodate the axisymmetric formulation of the dynamo model used for forecasting. Both aforecited model-based prediction schemes used distinct geometricaly simplified implementations of different datasets being assimilated, and in all likelihood these differences also contributed to the widely varying predictions for the amplitude of cycle 24. Ideally, data assimilation should be carried out using full-disk magnetograms and/or detailed observations of active region emergences, including complete positional and timing information. Either way, this requires a dynamo model with a geometrically complete representation of the solar surface, and thus demands abandoning axisymmetry.

One extreme possibility consists in turning to global magnetohydrodynamical simulations of solar convection. Despite remarkable progress in the past decade (for a review see, e.g., § 3 of Charbonneau 2014), such simulations still cannot accommodate sufficient spatial resolution to resolve convection and magnetic field evolution in the surface layers, or even capture the interior process of magnetic flux rope formation and buoyant rise (but on the latter do see Nelson et al. 2013; 2014). Typically, such simulations also fail to drive regular, solar-like polarity cyclic reversals in the large-scale magnetic field they generate (but see Passos & Charbonneau 2014 for the closest thing yet).

Intermediate approaches are also possible: finding a way to include the full non-axisymmetric representation of, at-least, the surface processes, while retaining the kinematic approach for the transport of magnetic flux. To our knowledge, only two such models exist in the literature (Yeates & Muñoz-Jaramillo 2013; Miesch & Dikpati 2014), as they include a full three-dimensional kinematic representation of the solar convection zone up to the surface. Here again, they mostly differ in how they incorporate the localized emergence of new magnetic flux: Yeates & Muñoz-Jaramillo (2013) impose localized flow perturbations at the base of the convection zone to trigger the eruption of active regions out of the toroidal flux, while Miesch & Dikpati (2014) apply a surface flux deposition technique, more alike our emergence procedure, through an empirical masking of the deep-seated toroidal field. [The models seem also to differ in the way they treat the surface boundary layer.]

In this series of paper we present a BL dynamo model that belongs to this same category. We retain a fairly conventional two-dimensional axisymmetric kinematic flux transport dynamo (FTD) model, specifically the model described in Charbonneau et al. (2005), without its non-local poloidal source term, and couple it to a two-dimensional surface flux transport (SFT) simulation. The latter provides the source term for the former through the upper boundary condition, and in turn the FTD provides the emergences required as input to the

SFT simulation. We opted to call this a "2 × 2D" dynamo model. This is still a kinematic model, in that it uses steady parametrized large-scale flow fields compatible with helioseismology and surface measurements. Specifying the form of these flows requires the adjustment of many model parameters, in order to generate the most "solar-like" dynamo solutions possible.

In Lemerle et al. (2015, hereafter Paper I) we introduced a genetic algorithm-based method for formally carrying out this optimization problem, in the context of the surface flux transport simulation. Not only does this approach finds the formally optimal solution, but it also allows to map a range of acceptable solutions, thus providing robust Monte Carlo-like confidence intervals on best-fit model parameters and allowing the identification of degeneracies in model parameters. Although the optimization process is set to minimize deviations with respect to synoptic magnetograms (and derived global quantities), the range of acceptable surface meridional flow profiles also fits nicely surface Doppler measurements (Ulrich 2010), even though these data are not used to constrain the optimization process.

In the present paper we extend the procedure to the coupled model described above, and thus produce an "optimal" 2 × 2D BL dynamo model of the solar cycle. The use of quotes is motivated by the fact that even this basic optimal model involves unavoidable stochastic components, associated with the flux emergence process, so that it can only fit the Sun (meaning, e.g., the sunspot number time series) in a statistical sense. Indeed, we also showed in Paper I how the uncertainties in global cycle characteristics were dominated by the inherent stochasticity of the flux emergence process.

In § 2 we discuss the formulation of the coupled model and its components. In § 3 we turn to its calibration against observed solar features. In § 4 we present self-consistent reference dynamo solutions and examine their long term patterns of variability. We conclude by comparing and contrasting our optimized 2 × 2D model to other BL-type dynamo models available in the extant literature.

2. MODEL

The contemporary version of the original picture proposed by Babcock (1959) runs as follows:

(0) at solar maximum, strong toroidal magnetic fields are present deep in the solar interior, antisymmetric with respect to the equator;

(i) during the ascending and descending phases of the solar cycle, toroidal flux loops rise and emerge at the solar surface in the form of BMRs, twisted due to the Coriolis effect, such that the western spots tend to be closer to the equator (tilt following on average the so-called Joy's law);

(ii) surface diffusion/transport near the equator allows for more cancellation of the western polarity, when merging with its opposite from the other hemisphere, leaving the remaining "eastern" flux to be transported toward the poles and to trigger the polarity reversal of magnetic polar caps;

(iii) the new surface dipole is subducted and sheared by differential rotation, building up a new internal toroidal magnetic structure, ready for

(iv) the generation of a new population of BMRs during the next half-cycle.

The numerical implementation we propose for carrying out this scheme is quite simple:

(i) new BMRs are continuously deposited at the solar surface, at times, latitudes and longitudes, tilts, angular separations, magnetic fluxes and polarity generated through a (probabilistic) flux emergence algorithm based on the strength and spatial distribution of the deep-seated magnetic fields;

(ii) the SFT equation is solved on the solar spherical surface, and generates the expected cancellation, decay, transport and specific features typically observed in surface magnetograms (see Paper I);

(iii) the FTD equation is solved in the meridional plane, using the evolving results of the surface simulation as a time-dependent upper boundary condition on the poloidal field; transport of this poloidal field to the base of the convection zone and subsequent shearing by differential rotation eventually builds up strong toroidal magnetic fields deep in the convection zone;

(iv) the dynamo loop is closed by allowing this deep-seated magnetic structure to generated the emergences required in step (i).

2.1. *Basic Ingredients*

In the depths of the solar convection zone or in the tangles of photospheric turbulent motions, magnetic fields are dispersed, transported, amplified or destroyed by small and large-scale flows. In the solar interior and photosphere, these processes are well-captured by the magnetohydrodynamics (MHD) induction equation:

$$\frac{\partial \boldsymbol{B}}{\partial t} = \boldsymbol{\nabla} \times (\boldsymbol{u} \times \boldsymbol{B} - \eta \boldsymbol{\nabla} \times \boldsymbol{B}) \,, \tag{1}$$

with η the net magnetic diffusivity, including contributions from the small microscopic magnetic diffusivity $\eta_e = c^2/4\pi\sigma_e$ (with σ_e^{-1} the electric resistivity of the plasma), as well as a dominant turbulent contribution associated with the destructive folding of magnetic field lines by small-scale convective fluid motions. We adopt here the kimematic approximation, whereby the flow $\boldsymbol{u}$ is considered given. This approximation has been shown to be appropriate in reproducing reasonably well the synoptic evolution of the solar surface magnetic field (see, e.g., Wang et al. 2002a; Baumann et al. 2004), as well as the overall solar dynamo properties (see, e.g., Karak et al. 2014, and references therein). On spatial scales much larger than convection, two flows contribute to $\boldsymbol{u}$: meridional circulation $\boldsymbol{u}_{\rm P}(r,\theta)$ and differential rotation $\varpi\Omega(r,\theta)\hat{\boldsymbol{e}}_\phi$. Both these flows can be considered axisymmetric ($\partial/\partial\phi \equiv 0$) and steady ($\partial/\partial t \equiv 0$) as per the kinematic approximation. They can be expressed in spherical

polar coordinates (r, θ, ϕ) as

$$\boldsymbol{u}(r,\theta) = \underbrace{\frac{R}{\rho(r)/\rho_0}\boldsymbol{\nabla}\times\left(\Psi(r,\theta)\hat{\boldsymbol{e}}_\phi\right)}_{\boldsymbol{u}_\mathrm{P}(r,\theta)=u_r(r,\theta)\hat{\boldsymbol{e}}_r+u_\theta(r,\theta)\hat{\boldsymbol{e}}_\theta} + \varpi\Omega(r,\theta)\hat{\boldsymbol{e}}_\phi \ , \quad (2)$$

where the meridional flow has been formulated in terms of a stream function $\Psi(r,\theta)$, thus ensuring mass conservation in a $\rho(r) = \rho_0\xi^m$ density profile, with $\xi(r) = (R/r) - 1$, $m = 1.5$ for an adiabatic stratification, R the solar radius, and $\varpi = r\sin\theta$.

2.1.1. *Meridional Circulation*

We opted to use a modified form of the meridional flow profile introduced by van Ballegooijen & Choudhuri (1988). This flow can be defined through a separable stream function of the form:

$$\Psi(r,\theta) = u_\theta(R,\theta)\frac{R}{r}\left[-\frac{\xi^{m+1}}{m+1}+\frac{c_1\xi^{2m+1}}{2m+1}-\frac{c_2\xi^{2m+p+1}}{2m+p+1}\right] , \quad (3a)$$

where

$$c_1 = \frac{(2m+1)(m+p)}{(m+1)p}\xi_b^{-m} \quad ,$$
$$c_2 = \frac{(2m+p+1)m}{(m+1)p}\xi_b^{-(m+p)} \ ,$$

and $\xi_b = (R/R_b) - 1$. Parameters p and m determine the depth and concentration of the return flow, down to $r = R_b$. For the purpose of the foregoing analysis and calibration, parameters p and R_b will be treated as free parameters, while m will keep the value of 1.5 characteristic of an adiabatic stratification.

We deviate from the original formulation of van Ballegooijen & Choudhuri (1988) by using the following latitudinal dependence, also used in Paper I:

$$u_\theta(R,\theta) = -\frac{u_0}{u_0^*}\,\mathrm{erf}^q\left(v\sin\theta\right)\,\mathrm{erf}^n\left(w\cos\theta\right) \ , \quad (3b)$$

with u_0^* a normalization factor such that u_0 is the maximum meridional flow velocity and q, n, v, and w parameters that allow to generate a very wide range of solar-like surface meridional flow profiles. The value of n is fixed to 1 as to prevent the formation of a 0 m s^{-1} plateau near the equator. We developed this flexible formulation in Paper I to allow for the inclusion of various profiles used in flux transport modeling (e.g., Dikpati & Charbonneau 1999; van Ballegooijen & Choudhuri 1988; Wang et al. 2002b) and measured on the Sun (e.g., Ulrich 2010).

2.1.2. *Differential Rotation*

Unlike meridional circulation, the solar internal differential rotation profile is well constrained by helioseismology. We use here the helioseismically-calibrated solar-like parameterization introduced in Charbonneau et al. (1999):

$$\Omega(r,\theta) = \Omega_c + \frac{\Omega(R,\theta)-\Omega_c}{2}\left[1+\mathrm{erf}\left(\frac{r-R_c}{\delta_c/2}\right)\right] \ , \quad (4a)$$

with $\Omega_c = 2.724$ μrad s^{-1}, $R_c = 0.7R$, and surface rotation

$$\Omega(R,\theta) = \Omega_0\left(1 + a_2\cos^2\theta + a_4\cos^4\theta\right) \ , \quad (4b)$$

where $a_2 = -0.1264$, $a_4 = -0.1591$, and $\Omega_0 = 2.894$ μrad s^{-1} (see also Snodgrass 1983). The thickness δ_c of the transition region between differential and solid rotation, the tachocline, near the base of the convection zone, is kept as a free parameter.

2.1.3. *Magnetic Diffusivity*

In the stably stratified core, the presumed absence of turbulence suggests a net diffusivity (η_c) given by Ohmic dissipation, while in the bulk of the convection zone, enhanced turbulent dissipation (η_t) of the magnetic field is expected to dominate. The following parametric profile, given by Dikpati & Charbonneau (1999), allows for a smooth transition between these two regions:

$$\eta(r) = \eta_c + \frac{\eta_t}{2}\left[1+\mathrm{erf}\left(\frac{r-R_c}{\delta_c/2}\right)\right] \ , \quad (5)$$

where R_c takes the same values as in the preceding differential rotation profile.

In the surface layer, supergranular convective motions drive a random walk that disperses magnetic flux, and can be modeled as a diffusive process (Leighton 1964) characterized by an effective magnetic diffusivity of order $\eta_R \simeq 10^{12} - 10^{13}$ cm^2 s^{-1}. This value is used solely in the SFT part of the model. The overall radial profile of $\eta(r)$ consequently includes an implicit step fonction at $r = R$. The exact values for η_c, η_t, and η_R, as well as δ_c, are virtually impossible to determine from first principles, such that they must be treated as a unknown parameter needing a proper calibration.

2.2. *The Flux Transport Dynamo Equations*

The large-scale axisymmetric magnetic field simulated in the FTD component of the model can be expressed as

$$\boldsymbol{B}(r,\theta,t) = \underbrace{\boldsymbol{\nabla}\times\left(A_\phi(r,\theta,t)\hat{\boldsymbol{e}}_\phi\right)}_{\boldsymbol{B}_\mathrm{P}=B_r\hat{\boldsymbol{e}}_r+B_\theta\hat{\boldsymbol{e}}_\theta} + B_\phi(r,\theta,t)\hat{\boldsymbol{e}}_\phi \ , \quad (6)$$

where $\boldsymbol{B}_\mathrm{P}$ and $B_\phi\hat{\boldsymbol{e}}_\phi$ are respectively the poloidal and toroidal vector components of the field. Inserting this decomposition for $\boldsymbol{B}$ along with Equation (2) for the flow, into the MHD induction equation (Equation (1)) then yields the usual two evolutionary equations for the scalar components $A_\phi(r,\theta,t)$ and $B_\phi(r,\theta,t)$:

$$\frac{\partial A_\phi}{\partial t} = -\frac{1}{\varpi}(\boldsymbol{u}_\mathrm{P}\cdot\boldsymbol{\nabla})(\varpi A_\phi) + \eta\left(\nabla^2 - \frac{1}{\varpi^2}\right)A_\phi \ , \quad (7a)$$

$$\frac{\partial B_\phi}{\partial t} = -\varpi(\boldsymbol{u}_\mathrm{P}\cdot\boldsymbol{\nabla})\left(\frac{B_\phi}{\varpi}\right) + \eta\left(\nabla^2 - \frac{1}{\varpi^2}\right)B_\phi$$
$$-(\boldsymbol{\nabla}\cdot\boldsymbol{u}_\mathrm{P})B_\phi + \frac{1}{\varpi}\frac{\partial\eta}{\partial r}\frac{\partial(\varpi B_\phi)}{\partial r} + \varpi\boldsymbol{B}_\mathrm{P}\cdot\boldsymbol{\nabla}\Omega \ . \quad (7b)$$

These two equations are linear in A_ϕ and B_ϕ, but are coupled by the shearing term in Equation (7a) which acts as a source for B_ϕ proportional to A_ϕ. No such source appears explicitly in Equation (7b). Here the regeneration and amplification of the poloidal field is supplied by a continuous input from the SFT simulation, providing a time-evolving surface boundary condition for A_ϕ which effectively acts as a source.

2.3. *Surface Flux Transport*

Following earlier modeling work on surface magnetic flux evolution, in particular in the preceding paper of this series (Paper I), we consider the magnetic field to be predominantly radial on global scales and we solve only the r-component of Equation (1), at $r = R$. This leads to the usual two-dimensional linear advection-diffusion equation for the scalar component $B_R = B_r(R, \theta, \phi, t)$,

$$\frac{\partial B_R}{\partial t} = -\frac{1}{R\sin\theta}\frac{\partial}{\partial\theta}\left[u_\theta(R,\theta)B_R\sin\theta\right] - \Omega(R,\theta)\frac{\partial B_R}{\partial\phi} + \frac{\eta_R}{R^2}\left[\frac{1}{\sin\theta}\frac{\partial}{\partial\theta}\left(\sin\theta\frac{\partial B_R}{\partial\theta}\right) + \frac{1}{\sin^2\theta}\frac{\partial^2 B_R}{\partial\phi^2}\right] - \frac{B_R}{\tau_R} + S_{\rm BMR}(\theta,\phi,t)\ , \quad (8)$$

to which two supplementary terms have been added: a source term $S_{\rm BMR}(\theta, \phi, t)$ to account for the discrete emergence of new surface flux in the form of BMRs, and a linear sink term $-B_R/\tau_R$ to allow for an exponential decay of the surface field with time. Schrijver et al. (2002) originally found such a decay on a timescale of $5 - 10$ years to be necessary to preclude secular drift and ensure polarity reversal of the polar cap when modeling surface flux evolution over many successive cycles of differing amplitudes. This was subsequently justified physically by Baumann et al. (2006) as the effect of a vertical turbulent diffusion, or equivalently a convective submergence, on the decay of the dominant dipole mode, two physical mechanisms that cannot be directly included in the SFT model. We included this term in Paper I but did not find it to be required for the SFT results to match the synoptic magnetogram of cycle 21. We test it again here, with τ_R treated as a free parameter.

2.4. *Numerical Solution and Coupling*

The FTD equations (7) and SFT equation (8) are solved concurrently, each on a separate two-dimensional computational grid on which spatial discretization is carried out via the Galerkin finite element method, and implicit temporal discretization through the one-step Θ-method (see, e.g., Burnett 1987).

The SFT simulation is solved over a regular Cartesian grid in (θ, ϕ) representing the whole solar surface, with longitudinal periodicity enforced through a padding of ghost cells. Rigorous flux conservation is also required since only a small fraction of the emerging magnetic flux ultimately builds up the axial dipole observed at sunspot minima. We minimize numerical discretization errors by adopting double precision arithmetics, a 256×128 longitude–latitude grid, and 8000 time steps for the eight-cycle runs that will be analyzed in this paper (for more details on numerical errors see Paper I, § 2.4 and figure therein).

The FTD simulation is solved simultaneously over a regular 128×96 Cartesian grid in $(r,\cos\theta)$, from pole to pole and $0.5 \le r/R \le 3.0$. Below $r = 0.5R$, the radiative core is considered perfectly conducting and the $A_\phi = B_\phi = 0$ boundary condition is applied. For $r > R$, the absence of flows and electrical currents imposes $B_\phi = 0$ and a potential field solution for A_ϕ: $\left(\nabla^2 - \frac{1}{\varpi^2}\right) A_\phi = 0$. The spherical geometry finally constrains $A_\phi = B_\phi = 0$ at the poles. The overall scheme is similar that described in (Charbonneau et al. 2005).

2.4.1. *From SFT to FTD*

The surface ($r = R$) boundary condition on A_ϕ is updated at every FTD time step, via the longitudinal averaging of the SFT solution $\langle B_R\rangle^\phi(\theta, t)$ and integration of the resulting latitudinal function:

$$A_\phi(R,\theta,t) = A_\phi^0 + \frac{R}{\sin\theta}\int\langle B_R\rangle^\phi(\theta,t)\sin\theta d\theta\ , \quad (9)$$

where A_ϕ^0 is set to zero at the poles. This provides the coupling from the SFT toward the FTD model.

2.4.2. *From FTD to SFT: Emergence Function*

The coupling from the FTD toward the SFT is the emergence of BMRs. In view of the considerable complexity of the various processes involved in the formation, destabilization, buoyant rise, and emergence of deep-seated magnetic flux tubes (see, e.g., Weber et al. 2011 and review by Fan 2009), we opted here to input emerging BMRs directly into the SFT component of the model, based on a semi-empirical emergence function giving, as a function of the strength of the internal magnetic field, the *probability* that the emergence of a BMR will occur.

Calculations of the destabilization and buoyant rise of magnetic flux tubes carried out in the thin-tube approximation do offer some useful guidance. From the stability diagrams obtained by Schussler et al. (1994) and Ferriz-Mas et al. (1994), one can infer the depth, latitude and magnetic amplitudes at which toroidal flux tubes are expected to destabilize. According to their results, and depending on the level of subadiabaticity, instability growth rates near $r/R \simeq 0.7$ remain approximately constant, or show a smooth increase with latitude, from the equator up to $\ell^* \simeq 70°$, and then fall of rapidly to zero in $\delta\ell^* \simeq 5°$. A lower threshold of order $10^4 - 10^5$ G is also required, on the amplitude of the magnetic field inside concentrated flux tubes. A crucial missing link is the degree of magnetic field amplification taking place during the formation of these toroidal flux tubes. Accordingly, we define this lower limit as $B^* \in 10^1 - 10^4$ G, and treat it as another free parameter to be calibrated. Modeling also shows that a certain level of twist is required for the tube to maintain its coherence during the rise through the convective envelope (Fan 2009). Accordingly, we introduce the quantity $|B_{\rm mix}| = |B_\phi|^b\,|A_\phi|^a$, with exponents in the range $b \in [0.5, 3.0]$ and $a \in [0.0, 2.0]$, and use it to build the following quasi-normalized emergence function:

$$|F_B(\theta,t)| = \frac{1}{4}\left(1 + {\rm erf}\left(\frac{|B_{\rm mix}| - B^*}{\delta B^*}\right)\right)\left|\frac{B_{\rm mix}}{\max|B_{\rm mix}|}\right|^c \times \left(\left(1-\mu_\ell\right)\frac{|\ell|}{90} + \mu_\ell\right)\left(1 - {\rm erf}\left(\frac{|\ell| - \ell^*}{\delta\ell^*}\right)\right)\ . \quad (10)$$

The first part of Equation 10 sets an emergence cutoff in $B_{\rm mix}$ below B^*, as well as a possible saturation ($c \to 0$) or linear growth ($c \to 1$) of the probability above B^*. The second part accounts for the latitudinal dependence of the instability's growth rate, which we assume to increase linearly from $\mu_\ell \in [0, 1]$ at the equator to 1 near latitude $\ell^* \ge 65°$, followed by a quick drop to zero (cf. Figures 1 and 2 in Ferriz-Mas et al. 1994). The sign of $F_B(\theta, t)$ is given by the sign of the input B_ϕ.

The emergence process is made inherently non-deterministic with the following sources of stochasticity:

(i) at every SFT time step, the relative number of new BMRs to emerge is extracted from a uniform random distribution, proportional to the sum $\sum_\theta F_B(\theta,t)$ at the corresponding FTD time step,

(ii) the probability of emergence of a BMR at a given latitude is made proportional to $F_B(\theta,t)$.

Also, independently from the distribution of $F_B(\theta,t)$, and as determined in our analysis of Wang & Sheeley (1989)'s database entries (see Appendix A of Paper I):

(iii) emergence longitudes are assumed to be random,

(iv) magnetic fluxes Φ are extracted from a log-normal distribution centered at $\log\Phi_0 = 21.3$ ($\log$ Mx) with standard deviation $\sigma_{\log\Phi} = 0.5$ ($\log$ Mx) (Paper I, Equation (13)),

(v) magnetic bipole separations δ follow a power law with flux, with a gaussian dispersion about it (Paper I, Equation (15)),

(vi) magnetic bipole tilts α relative to the equatorial direction follow a linear increase with latitude (Joy's law) and a gaussian spread with standard deviation decreasing exponentially with $\log\Phi$ (Paper I, Equations (16*a*) and (16*b*)).

The input of BMRs in the SFT simulation enter the source term

$$S_{\rm BMR}(\theta,\phi,t) = \sum_i B_i(\theta,\phi)\delta(t-t_i)\ , \tag{11a}$$

with δ the Dirac delta. Each new BMRs is placed at its given position (θ_i,ϕ_i) and time t_i, with a gaussian distribution for each pole:

$$B_i(\theta,\phi) = \underbrace{B_{i0}e^{-\delta_{i+}^2/2\sigma^2}}_{B_{i+}(\theta,\phi)} + \underbrace{-B_{i0}e^{-\delta_{i-}^2/2\sigma^2}}_{B_{i-}(\theta,\phi)}\ , \tag{11b}$$

where δ_{i+} and δ_{i-} are the heliocentric angular distances from the centres (θ_{i+},ϕ_{i+}) and (θ_{i-},ϕ_{i-}) of the two poles, respectively, and $\sigma = 4°$ the width of the gaussians.

The preceding steps dictate the relative probability of given emergences to occur, but the actual number of BMRs to emerge every time step remains adjustable. The conversion factor K, between the emergence function $F_B(\theta,t)$ and the actual emerged butterfly diagram, eventually sets the absolute amplitude of the dynamo. It therefore plays the role of a dynamo number.

These distributions of BMRs emergence, i.e. the SFT source term, is a most critical aspect of the 2×2D BL dynamo model. In order for it to match the solar dynamo behaviors, the next logical step is to carry out a calibration of all parameters describing the full model, using observed emergences as a contraint, as detailed in the following section.

3. MODEL CALIBRATION

The various physical components of the coupled FTD+SFT model introduced in the preceding section jointly involve a large number of numerical parameters; 27 to be precise. Nine of these can be fixed confidently either through observations or theoretical considerations. Five (r_c, Ω_0, Ω_c, a_2, and a_4) are the numerical parameters defining the differential rotation profile (see § 2.1.2), another (m) is the polytropic index characterizing the stratification within the convection zone, and yet another (n) is used to formulate a flexible surface meridional flow profile but set to 1 to reflect solar observations (see § 2.1.1). The last two parameters to be held fixed, δB^* and $\delta\ell^*$, control the *Alex:* ~~sizes of each member of the BMR injected on the model photosphere~~ shapes of the latitudinal and magnetic masking used in the emergence function (see § 2.4.2); experimenting with the model reveals that within reasonably wide ranges, the exact values chosen for these parameters have little impact on the global dynamo behavior. Consequently, they are fixed at values $0.1B^*$ and 5° respectively.

This leaves 18 adjustable parameters, which are listed in Table 1. Eleven pertain to the linear terms in the model, including the shape of the meridional flow, magnetic diffusivity and surface sink (δ_c, R_b, u_0, p, q, v, w, η_c, η_t, η_R, and τ_R), and the remaining seven (r^*, b, a, c, B^*, ℓ^*, and μ_ℓ) to the form of the nonlinear emergence function (§ 2.4.2).

3.1. *Validation Against the Miesch & Dikpati 2004 Model*

The large number of model parameters listed in Table 1 results from the very general forms adopted for many model ingredients, notably the meridional flow profile and emergence function. This gives the model great flexibility, in that it includes as a subset a number of published models. As an example and a form of validation exercise, we now reproduce a dynamo solution resembling to the one presented in Miesch & Dikpati (2014).

Since Miesch & Dikpati (2014)'s model includes a full two-dimensional representation of the solar surface and an emergence algorithm similar to ours, direct contact is allowed between specific features of the two models [except for different numerical procedures]. Their [single-cell] meridional circulation profile (described in Dikpati 2011) and magnetic diffusivity profile (described in Dikpati & Gilman 2007) may be closely approached by ours, provided the parameter values listed in the first column of Table 1. Similarly, their emergence function is comparable to the one we describe in § 2.4.2, with a latitudinal masking approximated by parameters $\mu_\ell = 0$ and $\ell^* = 45°$ (a low-latitude cutoff conducive to the production of a solar-like butterfly diagram but hard to justify from the point of view of stability of thin flux tubes) and applied to the B_ϕ component only evaluated at depth $r^*/R \simeq 0.705$. The magnetic masking includes a lower threshold B^* of unknown value and apparently no higher threshold (parameter c) (see first column of Table 1). The detailed parametrization of individual emerging BMR nonetheless differs significantly from ours, in a generally more deterministic manner. The latitude of emergence is directly associated with the location of peak toroidal field, as compare to the probabilistic approach

Table 1
Parameter values

Symbol	Reference value ($C = 0.28$)		Tested interval	Optimal solution ($C \in [0.90, 0.95]$)
δ_c/R	0.05		[0.04 , 0.10]	0.08 ± 0.01
R_b/R	0.69		[0.60 , 0.70]	$0.600 \pm {}^{0.005}_{0.000}$
u_0	18	[c]	[8 , 18]	17 ± 2 m s^{-1}
m (remove)	0.5		[0.4 , 2.0]	$\mathbf{1.5} \pm {}^{0.3}_{0.2}$
$\log p$	2.0		[−1.0 , 1.0]	-0.6 ± 0.4
q	2.5	[d]	[2^0 , 2^5]	$\mathbf{0} \pm {}^{1}_{0}$
v	1.0	[d]	[2^0 , 2^3]	$\mathbf{0} \pm {}^{1}_{0}$
w	3.5	[d]	[2^0 , 2^5]	$\mathbf{0} \pm {}^{1}_{0}$
$\log \eta_c$	9		[7 , 11]	$9 \pm \frac{1}{2}$ (cm^2 s^{-1})
$\log \eta_t$	10.7		[11.0 , 13.0]	11.8 ± 0.1 (cm^2 s^{-1})
$\log \eta_R$	12.48	[c]	[12.38 , 12.82]	350 ± 150 (cm^2 s^{-1})
τ_R	[a] 32	[c]	[7 , 32]	8 ± 4 years
r^*/R	0.705		[0.60 , 0.70]	$0.600 \pm {}^{0.005}_{0.000}$
b	1.0		[0.5 , 3.0]	$\mathbf{1.0} \pm {}^{0.1}_{0.2}$
a	0.0		[0.0 , 2.0]	$\mathbf{0.0} \pm {}^{0.1}_{0.0}$
c	1.0		[0.0 , 1.0]	$\mathbf{1.0} \pm {}^{0.0}_{0.6}$
B^*	[b] 10^2		[10^1 , 10^4]	$\mathbf{2} \pm 0$ G
ℓ^*	45		[64 , 90]	$0.600 \pm {}^{0.005}_{0.000}$
μ_ℓ	0.0		[0.0 , 1.0]	$0.600 \pm {}^{0.005}_{0.000}$

Note. — [INTERVALLES, LOG, UNITES A CORRIGER] Reference values approximate velocity and diffusivity profiles, and emergence procedure used by Miesch & Dikpati (2014). profiles are the ones used for the solution shown in Figure 1d. Intervals given for each parameter are those used for optimizations W21×8-18 and W21×8-11. Final solution is given after the last W21×8-11 optimization, with following error analysis. Values in bold were manually fixed prior to this last optimization.

[a] $\tau_R \gtrsim 32$ years is equivalent to removing term $-B_R/\tau_R$ in Equation (8).

[b] Threshold value B^* unavailable from Miesch & Dikpati (2014).

[c] As determined in Paper I, where the initial interval were $u_0 \in [5, 30]$ m s^{-1}, $\eta_R \in [10^2, 10^4]$ km^2 s^{-1}, and $\tau_R \in [2^1, 2^5]$ years. The linear correlation between u_0 and η_R obtained from the surface analysis should still be considered in [conjunction] with the final results given in the rightmost column.

[d] As opposed to the optimal intervals obtained in Paper I, where $w = 8 \pm {}^{2}_{4}$, $v = 2.0 \pm {}^{1.5}_{1.0}$, and $q = \left(2.8 \pm {}^{2.0}_{1.1}\right) \cdot 2^{1.25(\log_2 v)^2}$.

we use. The tilts, separation, sizes and fluxes of the spot pair seem to be mainly determined by the value of B_ϕ and the latitude of emergence, rather than associated with independent statistical distributions. [Both approaches have their weaknesses.]

In order to minimize the differences associated with stochastic realizations of our emergence procedure, we limit this exercise to the input of observed emergences. Following Paper I, we use the comprehensive database of over 3000 BMRs gathered by Wang & Sheeley (1989) for cycle 21. By feeding these data into Equations (11a) and (11b), the 2 × 2D simulation is indirectly forced to run in a cycle-21-like mode. The remaining model parameters are set to approach Miesch & Dikpati (2014)'s model (first column of Table 1). We obtain the two-cycles solution presented in Figure 1(a), for the synoptic evolution of B_ϕ at the base of the convection zone. This solutions resembles Miesch & Dikpati (2014)'s result in that it presents a strong mid-high-latitude poleward branch, as well as a weaker low-latitude equatorial branch.

Applying the appropriate latitudinal and magnetic mask, we obtain the emergence function, or equivalently the probabilistic distribution of emergences, presented in Figure 1(b). Unfortunately, this result does not match solar observation in the sense of producing the butterfly diagram of emergences. We now seek to better match the solar dynamo behaviors by adjusting model and masking parameters in a rigorous way.

3.2. *Numerical Optimization*

We are now facing the monumental task which consists in optimizing the 18 parameters listed in Table 1 so that the resulting magnetic field evolution most closely resembles solar observations.

The first choice to be made is the goodness-of-fit measure to be used to drive such optimization. We opted to use a single fitness measure, namely the value of the correlation coefficient C between the synoptic distribution of synthetic and observed emergences of BMRs. This presupposes that the magnetic flux tubes producing BMRs upon emergence through the photosphere rise radially through the convection zone, on a timescale very much shorter than the cycle period, [comparable with the used numerical time steps]. Models based on the thin flux tube approximation support this idea, at least for the more strongly magnetized flux tube presumably producing the larger BMRs (see, e.g., Fan 2009, and references therein).

Next we must select a suitable observational dataset against which to optimize the model.

Following Paper I, we use the comprehensive database of over 3000 BMRs gathered by Wang & Sheeley (1989) for cycle 21. By feeding these data into Equations (11a) and (11b), the 2 × 2D simulation is indirectly forced to run in a cycle-21-like mode. In order to minimize any influence of the initial condition (solar minimum-like dipolar configuration, as introduced in Paper I), we generate a sequence of eight replications of the cycle 21 database (hereafter W21×8), by sequentially inverting the latitudes of emergence from one replication to the next, and use the output corresponding to the last two cycles to compute the correlation coefficient.

We perform the numerical optimization of C using the genetic algorithm-based optimizer PIKAIA 1.2[c0] (Charbonneau & Knapp 1995; Charbonneau 2002). Genetic algorithms allow for an efficient and adaptive exploration of the parameter space, and are thus quite robust at handling global optimization problems. As described in Paper I, they also allow for a quasi-Monte Carlo sampling of the parameter space about the current optimum solution, thus helping to construct error estimates on optimal parameter values. In the present context PIKAIA is operating in a 18-dimensional parameter space (viz. Table 1), with the fitness measure given by the correlation C. As numerical optimization algorithms, genetic algorithm (GA) tend to be computationally expensive, as the number of model evaluations is equal to the population size times the number of generational iterations. In most model fitting tasks reported upon in what follows, a population size of 96 trial solutions evolving over

[c0] http://www.hao.ucar.edu/modeling/pikaia/pikaia.php (March 2015)

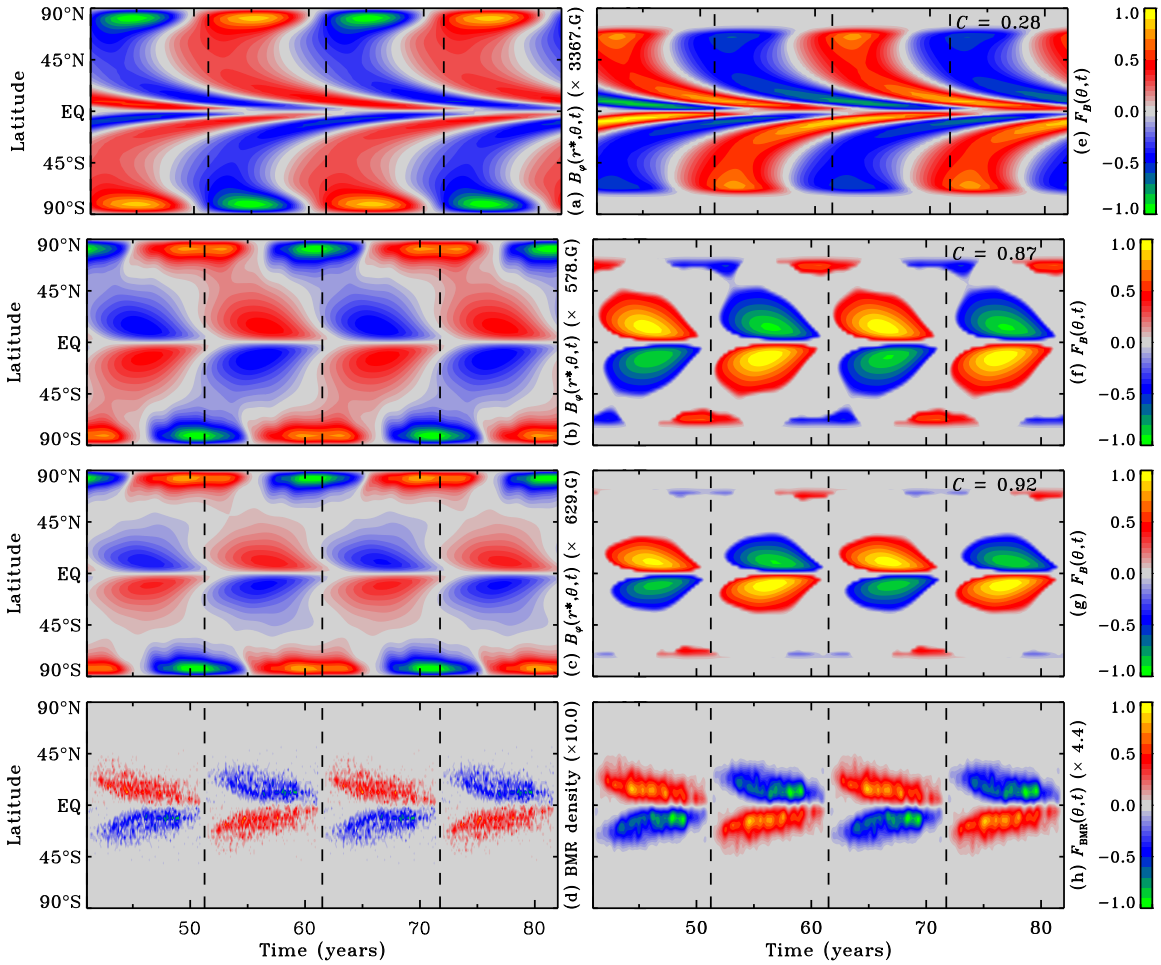

Figure 1. [FIGURES A METTRE A JOUR] Left: Time-latitude contour plots of the toroidal magnetic field component $B_\phi(r^*,\theta,t)$, averaged between $r^*/R = 0.68$ and 0.70, for a) a reference solution run over two replications of solar cycle 21, c) an optimal, but unacceptable, solution ($C = 0.86$) found within the limits imposed by the surface optimization of Paper I, e) an example of an acceptable solution with $C = 0.90$, and g) an optimal solution ($C_{\max} = 0.95$). i) Density plot of observed BMRs, extracted from Wang & Sheeley (1989)'s database, where all emergences in a given hemisphere and cycle have been attributed the same polarity. Right: b,d,f,h) Time-latitude contour plots of the emergence function $F_B(\theta,t)$ associated with each of the solutions presented at the left, with corresponding linear correlation coefficients. j) Smoothed version of the density plot presented at the left. All diagrams show the last quarter of simulations W21×8 (last two repetitions of cycle 21), which was used for optimization. Time, given in years, starts at the beginning of the eight-cycles runs. Vertical dashed lines indicate the times of activity minima.

500 generations was found to be sufficient to reliably ensure proper convergence of all model parameters. This adds up to 48000 model fitness evaluations per optimization run. Calculating the fitness of a single trial solution (18-parameter vector) implies running the SFT and FTD simulations in parallel, with appropriate coupling through the surface boundary condition, and finally evaluating C. For our working spatial mesh and time stepping this requires about twenty minutes on a single-core modern CPU, adding up to 667 core-days for a typical optimization run. However, this sequence of operations is applied independently to each member of the population, and so can easily be carried out in parallel (see, e.g., Metcalfe & Charbonneau 2003). With the only information returned by each evaluation being the fitness, near-perfect parallelization can be achieved, by assigning one core per population member, thus bringing the wall-clock time down to a few days.

3.3. *Choosing Parameter Ranges*

The intervals explored for each parameter (second column of Table 1) are chosen to be physically meaningful and computationally stable.

[...]

[In particular, parameters u_0 and η_R are restricted to the intervals found in Paper I to better reproduce surface synoptic magnetograms. Parameters q, v, and w are left free to vary in their full original intervals despite the preceding calibration.]

For masking parameters, we use values within ranges allowed by instability diagrams [REF], as mentioned earlier, which means excluding the $\ell^* = 45°$ value used by Miesch & Dikpati (2014).

[...]

3.4. *Optimal Solution for Cycle 21*

Paul: [Describe optimal solutions...]

Alex: [J'attendrais plutot la fin de la section...]

The first sequence of optimizations are run with all 18 unconstrained parameters allowed to vary freely in the in-

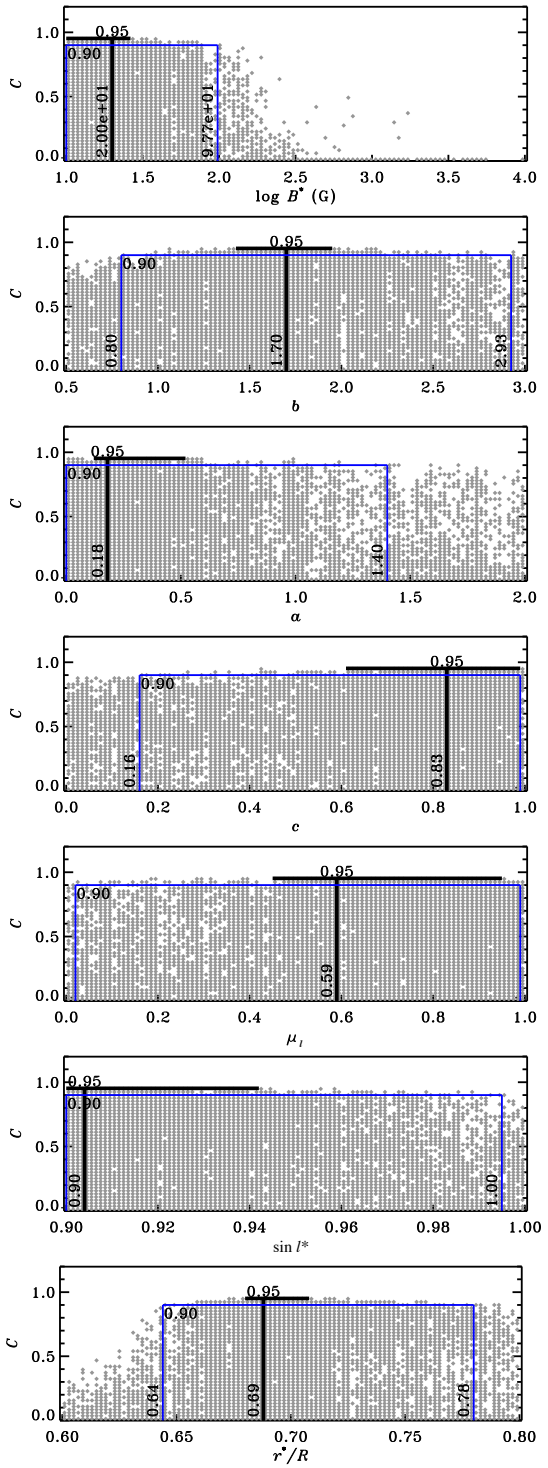

Figure 2. [TRY LOG SCALE, ADD W21×8-18 CAPTIONS IN THE FIGURES, CHANGE PARAMETERS ORDER: r^*, b, a, c, B^*, ℓ^*, and μ_ℓ.] Fitness C as a function of emergence parameters, for each of the 43200 solutions obtained from three independent optimizations of the W21×8-18 set. On each plot, the thick horizontal line indicates the interval where $C \geq 0.950$, and the thick vertical line the parameter value where true maximum fitness $C = 0.955$ is reached. Thin vertical blue lines indicate the parameter values where fitness reaches $C = 0.90$, such that any solution above the horizontal blue line is considered acceptable.

tervals listed in Table 1, hence called W21×8-18. We first analyse the model's behavior relative to the parameters involved in the very definition of the emergence function $F_B(\theta, t)$ (Equation (10)). Figure 2 illustrates the value of the goodness-of-fit C as a function of emergence parameters r^*, b, a, c, B^*, ℓ^*, and μ_ℓ for a set of 43200 solutions obtained from three independent optimizations (different seed populations), 200 generations each, 72 members per generation. In all three optimizations, the fitness reaches the same optimal value $C_{\max} = 0.95$, surrounded by a wide variety of sub-optimal solutions and of unacceptable ones.

Clearly, all seven parameters presented are not equally constrained by the fitting procedure. By looking at all solutions standing above the $C \geq 0.950$ (thick black) line, we get a first estimate of the relative restriction applied on each parameter. For instance, parameters r^*, b, a, and B^* appear fairly well constrained to a limited interval within the original boundaries, while parameters c, ℓ^*, and μ_ℓ show wider valid regions.

In order to build meaningful [strongly motivated] error estimates for each parameter, we must assess the physical limit of validity of the optimization criterion. In such a complex modeling problem, the optimal solution is only as physically meaningful as the goodness-of-fit measure being maximized by the GA. Our adopted fitness measure is physically motivated, but nonetheless retains some level of arbitrariness (e.g., ...). Clearly, there must exist a value of C above which solutions are physically acceptable, even if not strictly optimal. An example of such a solution, with $C = 0.90$, is presented in Figures 1e and 1f. The butterfly shape in this solution is still clearly visible, though a second tail is starting to build towards the high latitudes. [...] These differences appear significant enough to understand that such solution is not as good as the optimal one, but still at the limit of acceptability in terms of observed global features. The horizontal blue lines on Figure 2 delimit the solutions that are characterized by a criterion $C \geq 0.90$. Only a few [...]% of all the solutions stand above this line, arising from various combinations of parameters inside the corresponding intervals (as delineated by the thin blue lines on the figure).

Before going further into the parameters analysis, we now opt to get rid of the variability associated with the definition of the empirical emergence function (Equation (10)), and pick up definitive values, within the interval of acceptability, for the parameters involved. The inferred depth for the generation of flux instabilities is thus set to its optimal interval $r^*/R = 0.70 \pm 0.02$, by averaging the magnetic field values between $r/R = 0.68$ and 0.72. For simplicity, the relative contribution to $B_{\rm mix}$ of the poloidal field is set to zero ($a = 0$), while we round the optimal exponent of the toroidal contribution to $b = 1.5$. The lower threshold, above which this diffuse toroidal field is assumed to be able to generate instabilities, is set to its highest acceptable value: $B^* = 10^2$G. The emergence function F_B remains proportional to $B_{\rm mix}$, with $c = 1.0$, rather than saturating above B^*. The highest latitude of emergence is fixed to $\ell^* = 70°$ ($\sin \ell^* = 0.94$), in accordance with instability diagrams by Ferriz-Mas et al. (1994), and the equatorial intercept μ_ℓ is set to 1.0, such that no latitudinal filter is applied below $\ell^* = 70°$, i.e. the probability of emergence

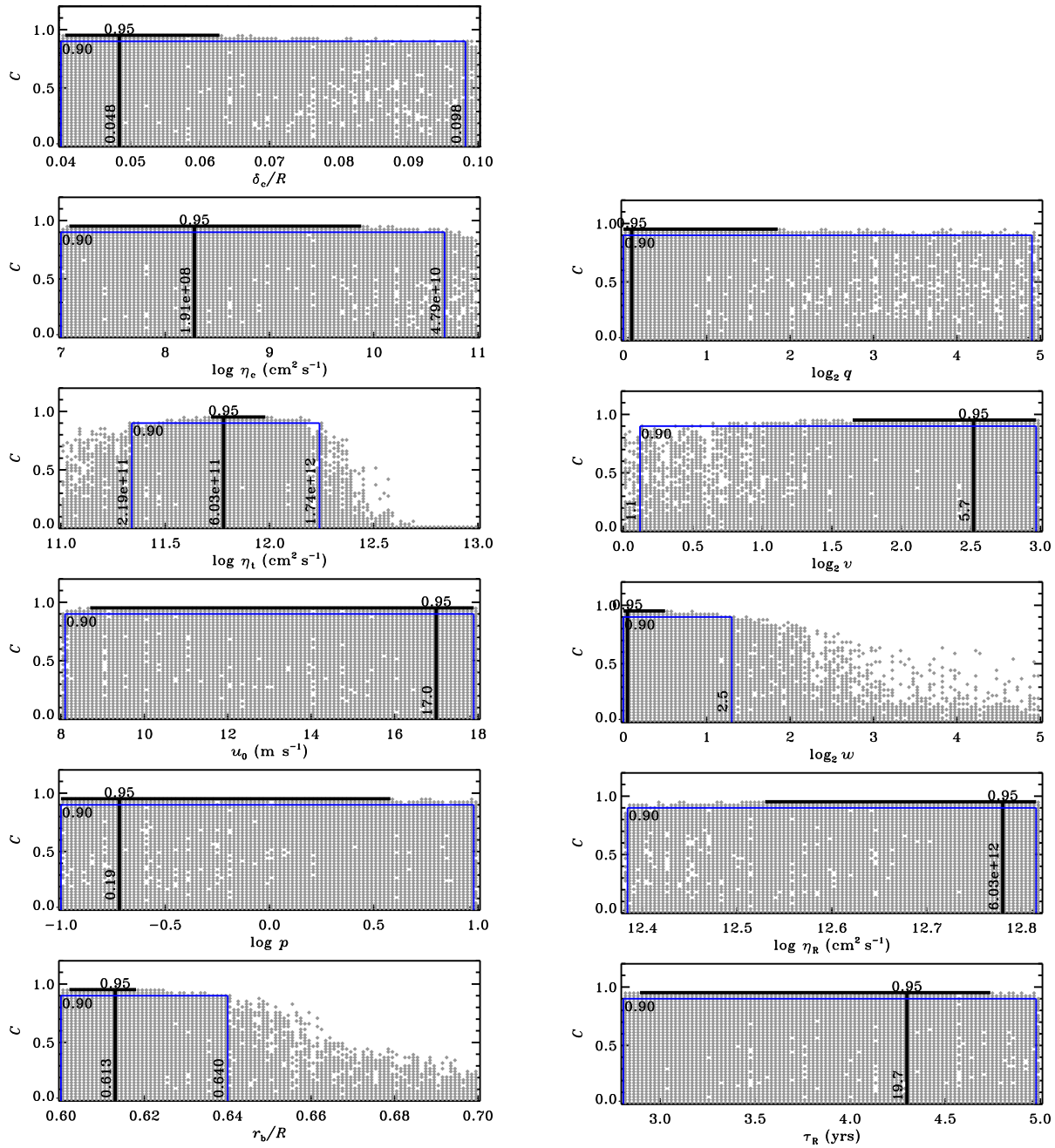

Figure 3. [ADD W21×8-11 CAPTIONS IN THE FIGURES] Same as Figure 2, but for the eleven physical model parameters, and three independent optimizations of the W21×8-11 set.

is only dependent on the value of $B_{\rm mix}$ at these latitudes.

The final emergence function (i.e. emergence probability) can now be mapped as a function of latitude and toroidal field amplitude, to form a synthetic "stability" diagram similar to the one presented in Ferriz-Mas et al. (1994) (Figure **??**). [FIG: SYNTHETIC STABILITY DIAGRAM]

That set, we carry out a new series of three optimizations, hereafter called W21×8-11, with only the 11 physical model parameters (δ_c, R_b, u_0, p, q, v, w, η_c, η_t, η_R, and τ_R) left to vary freely in their prescribed intervals. The corresponding 43200 solutions are presented on Figure 3 as a function of each parameter values. Again, the optimal fitness reaches $C_{\rm max} = 0.95$, and all solutions characterized by a $C \geq 0.90$ are considered acceptable. The corresponding interval for each parameter is used to define final error bars about the optimal value, as listed in the last column of Table 1. As mentioned earlier, various combinations of parameters within these accepted intervals lead to acceptable solutions, but not all. These results should therefore be used in conjunction with an understanding of the shape of the parameter-space landscape in the optimal region. Among the 55 possible two-dimensional cuts of the domain, ten are presented on Figure **??**. [FIG OF CORRELATIONS BETWEEN PARAMETERS ?] Some parameters present specific regions of validity, while others show nearly filled rectangles indicating that all combinations are valide within the final

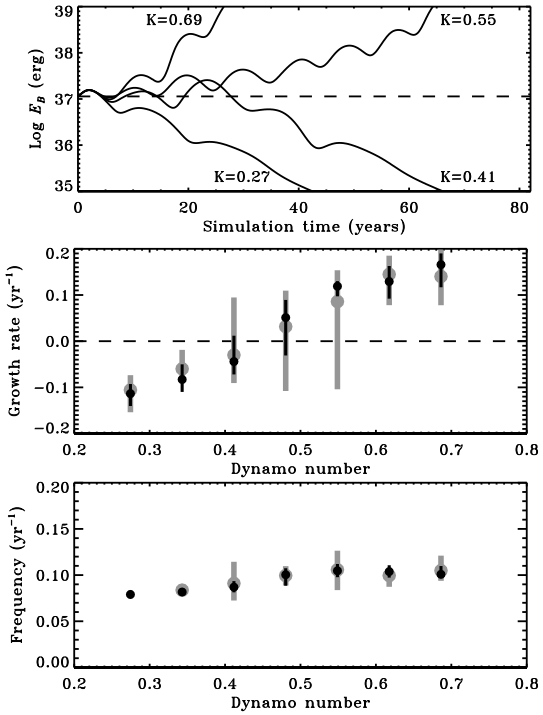

Figure 4. Top panel: evolution of the total magnetic energy content inside the simulated Sun, for ≃ 8-[half]-cycles sample realizations of a 2 × 2D dynamo run in the quasi-linear regime at four different dynamo numbers K (horizontal dashed line indicates the initial energy level). Middle panel: long term growth rate of the magnetic energy as a function of dynamo number K, ten independent realizations per value of K, both in the fully stochastic (thick grey) and partially stochastic (thin black) regimes. Bottom panel: similar as the preceding panel, but for the oscillating frequency of the detrended magnetic energy.

interval.

4. A SOLAR-LIKE DYNAMO SOLUTION

Now that the physical model and masking parameters have been properly calibrated to ensure that function $F_B(\theta, t)$ reproduces the observed solar butterfly diagram of surface emergences, we may use it as the statistical emergence function it was meant to be, i.e. feeding the missing surface source term $S_{\rm BMR}(\theta, \phi, t)$ (Equations (11a) and (11b)) with new emergences generated from deep seated toroidal flux and thus closing the loop for a self-consistent 2 × 2D dynamo.

In all following cases, we use as initial condition the simulation state at the end of the previously calibrated W21×8 sequences. This ensures that the new simulations start up from an adequate state not so far from a solar activity minimum.

4.1. *Quasi-Linear Regime*

The quasi-linearity in $\boldsymbol{B}$ [...] of the FTD equations (7a) and (7b) and SFT equation (8) is expected to generate either growing or decaying dynamos. As in the well-studied mean-field framework where this behavior is controlled by the level of alpha-effect *Alex:* [Je n'utilise pas le symbole α car il est utilise dans l'article pour les tilts] provided, it is here the conversion factor between $F_B(\theta, t)$ and the surface butterfly diagram, i.e. the absolute number of emerging BMRs, that plays the role of such a "dynamo number". The top panel of Figure 4 illustrates the temporal evolution of the total magnetic energy content inside the simulated Sun, for ≃ 8-[half]-cycles sample realizations of a 2 × 2D dynamo run in the quasi-linear regime at four different dynamo numbers K. From these few samples, the transition between decaying (small K) and ever growing (large K) solutions seems sharp, but a more complete analysis reveals otherwise. The middle panel of Figure 4 shows how the growth rate of the magnetic energy varies no so regularly with K. Error bars on the plot illustrate the intervals of growth rates obtained at each given K, through ten different realizations of the statistical emergence procedure described above, in both fully stochastic (RAPPELER LES SOURCES sources (i) to (vi)) and partially stochastic regimes (RAPPELER LES SOURCES sources (i) to (iv) only). This reveals the rather high level of stochasticity [non-linearity] introduced by these random processes, a expected characteristic of BL dynamo models [REF], in particular the distributions in separations (v) and tilts (vi) of emerged BMRs. The consequence is that bifurcation occurs over some interval, rather than on a well-defined point, with different realizations of the dynamo in $K \simeq [0.4, 0.6]$ resulting in diverging results. The fact that this transition region lies near one half of the reference value $K = 1.0$ (by definition required through the calibration of the preceding section to reproduced the observed butterfly diagram for cycle 21) suggests that the dynamo should run in a strongly supercritical regime, with some non-linear feedback operating. This aspect will be discussed in the following subsection.

As another indicator of the model behavior, average cycle frequencies (periods) of the corresponding solutions, are also presented in the bottom panel of Figure 4, again with error bars showing the intervals of frequencies obtained for a given K. Considering the imprecision at measuring cycle periods for quickly decaying dynamos (low K), no strong trend appears from this plot. This suggests how robust is the model at producing oscillations on a $10 - 11$ years timescale, in spite of the strong variability associated with stochastic processes.

4.2. *Tilt-Quenching and Reference Dynamo Solution[s]*

To overcome the problem of linearity, but without dealing explicitly with dynamical feedback, some ad hoc quenching may be added to the dynamo source terms. As would the well-known mean-field alpha-quenching do, we apply here a tilt-quenching relative to the amplitude of the contributing underlying toroidal field $B_\phi(r^*, \theta, t)$, in order to mimic the inertia of strong rising flux tubes against the twisting imparted by the Coriolis force. The quenched tilt is written

$$\alpha_q = \frac{\alpha}{1 + (B_\phi / B_q)^2} \ , \tag{12}$$

with B_q some ajustable critical magnetic field amplitude. In the context of the present dynamo model, we find a tilt-quenching with $B_q \simeq 500$ G, at dynamo number $K = 0.75$, to be adequate to generate stable dynamos, comparable to solar amplitudes for the butterfly density plot and the monthly number of newly-emerged BMRs (or "pseudo-SSN"). *Alex:* [Describe how it differs from the SSN...] The value $K = 0.75$ is still behind the $K = 1.0$ that was used in the calibration process. This could

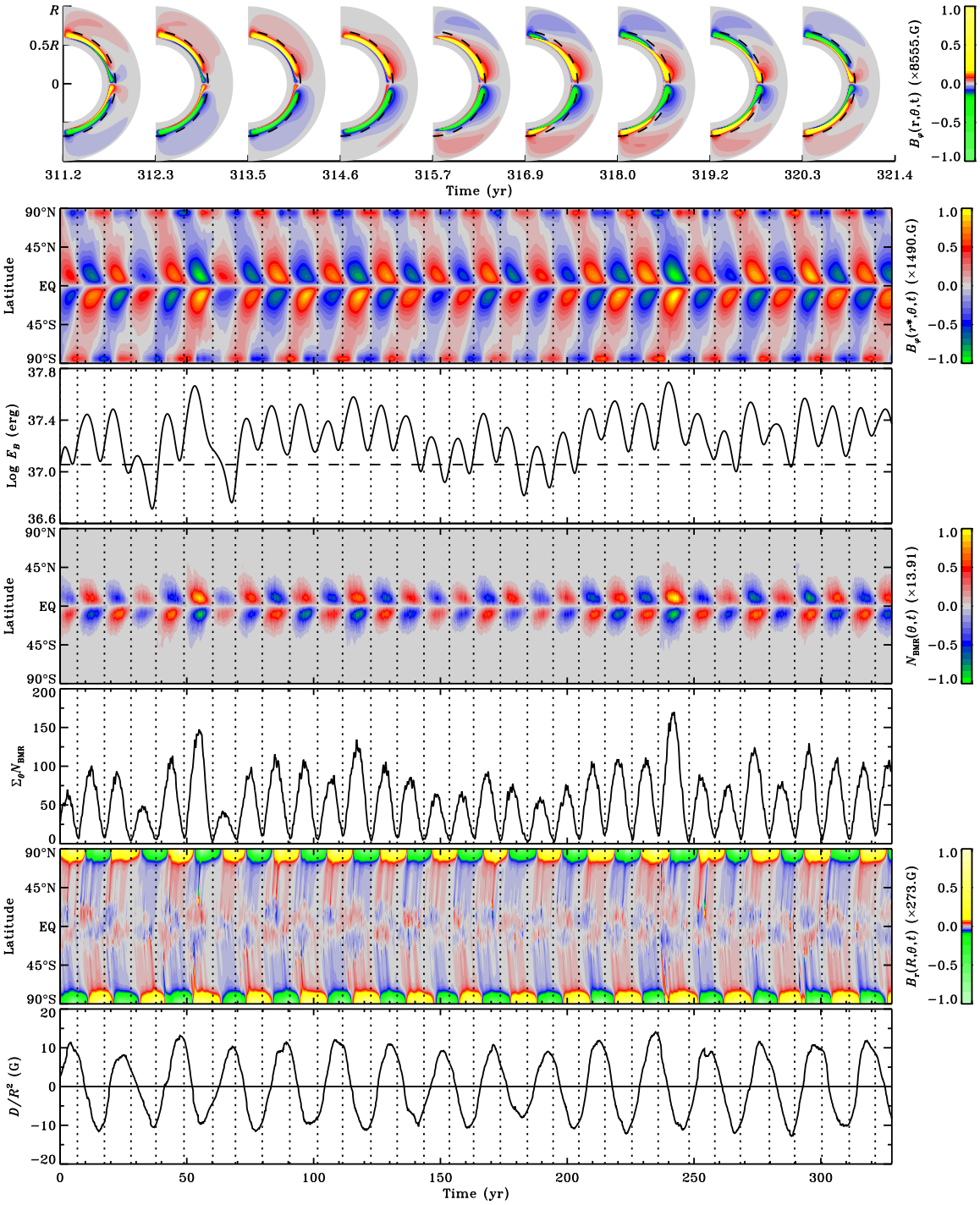

Figure 5. [NUMEROTER !!] From top to bottom: latitude–radius snapshots of the toroidal magnetic field between $r/R = 0.5$ and 1.0, at nine different phases of one of the following half dynamo cycles (color table saturated above 1.5 kG), with dashed lines indicating the depth of the tachocline ($r/R = 0.7$); time–latitude contour plot of the toroidal magnetic field averaged in the depth range $0.68 \leq r^*/R \leq 0.72$, for a $\simeq$ 32-[half-]cycles (more than 300 years) realization of a tilt-quenched 2×2D dynamo, run at supercritical dynamo number $K = 0.75$; corresponding temporal evolution of the total magnetic energy content inside the simulated Sun ($0.5 \geq r/R \geq 1.0$), with horizontal dashed line indicating the initial energy level; time–latitude density plot (butterfly diagram) of the number of BMRs emerged at the surface, as dictated by the emergence function F_B, in turn based on the preceding toroidal field amplitude; corresponding monthly number of newly emerged BMRs (pseudo-SSN), as a function of time; time–latitude contour plot of the surface radial magnetic field (color scale saturated above 27 G); and corresponding temporal evolution of the surface axial dipole moment. Vertical dotted lines indicate the times of activity minima as defined by the minimum values of the pseudo-SSN.

suggest an inappropriate absolute amplitude for the dynamo, but these considerations are of minimal importance in the present context where we seek only the general behavior of the dynamo. A calibration of this nature will likely be required, however, in [the] following paper of this series where we plan to study the predictive capability of the model for forecasting solar activity.

Figure 5 illustrates the evolution of the deep toroidal field, total magnetic energy, BMRs density, pseudo-SSN, surface radial field, and axial dipole moment for a sample dynamo solution run over more than 300 years and roughly 32 synthetic solar [half-]cycles. The temporal series illustrate solar-like behaviors in many aspects, in particular cycle periods varying between 8.5 and 12 years, cycle amplitude variations of a factor three to four in the pseudo-SSN, and long term variability such as some progressive increase of cycle amplitude after the occurence of a weak cycle or the triggering of small cycles after very strong ones. Some significant hemispheric asymmetries are also noticeable on the various plots, but still with a sharp synchronization which indicates a strong coupling between hemispheres. On the other hand, monthly fluctuations of the pseudo-SSN appear weaker than those of the Sun, revealing some deficiencies in the stochasticity of the flux emergence process. The amplitude of the oscillating surface axial dipole moment also peaks at too high values ($\simeq 10$ G) as compared with the Sun ($\simeq 4$ G at the end of cycle 21). This is due to either a surplus of emerged flux induced by too high a value for K or most probably to the use of a suboptimal profile for the surface meridional circulation leading too extra flux accumulation near the poles. The peak amplitude of the radial surface field, systematically located near the poles at activity minima, is in fact an order of magnitude stronger than the observed one.

Also shown in Figure 5 is a series of radius–latitude cuts of the toroidal field component, at nine different phases of a synthetic sunspot cycle. The toroidal field reverses amplitude after $\simeq$ 9 years, which is slightly shorter than the average observed sunspot cycle. The peak toroidal field amplitude near $r/R = 0.7$ is reached at mid-cycle, near maximum sunspot activity. Below the tachocline, the magnetic field from three to four successive cycles piles up to thinner and thinner layers as it reaches the depth $r/R = 0.6$. This is precisely what is to be expected from the average diffusivity $\eta \simeq 5 \times 10^{10}$ cm^2 s^{-1} used in $0.6 \geq r/R \geq 0.7$, which corresponds to a diffusive time-scale of $\simeq 31$ years. Below $r/R = 0.6$, the magnetic diffusivity set to 10^9 cm^2 s^{-1}, leads to a diffusive time-scale $\gtrsim 1000$ years. Therefore, while the meridional circulation acts on a time-scale commensurate with the sunspot cycle period, the deep diffusive processes act on much longer terms. The remnants from old cycles appear to be able to feed back into the dynamo system and induce long term memory.

Figure 6 shows some long term interrelations between cycle properties, extracted from the preceding dynamo solution. The middle left panel in the figure illustrates the strong linear correlation (0.89) obtained between cycle (n) amplitude (maximum pseudo-SSN) and maximum axial dipole moment at the end of the preceding cycle ($n-1$). This behavior is to be expected from the quasi-linear transport and conversion of the poloidal magnetic energy accumulated at cycle minimum into a deep toroidal component peaking at cycle maximum and generating a proportional number of surface emergences. As shown in the middle right panel of the figure, the reverse correlation is not true, however, as the stochastic properties of emerged BMRs during a given cycle n prevent a direct determination of the axial dipole amplitude at the end of the same cycle (n). Also, even if long term memory does exist in the system, the bad correlations obtained between amplitude of cycle n and axial dipole at the end of cycles $n-2$ (top right panel) and cycles $n-3$ (top left panel) show how these processes are not completely deterministic. All the preceding results correspond precisely to the observed solar cycle characteristics (see, e.g., Muñoz-Jaramillo et al. 2013, Figure 5).

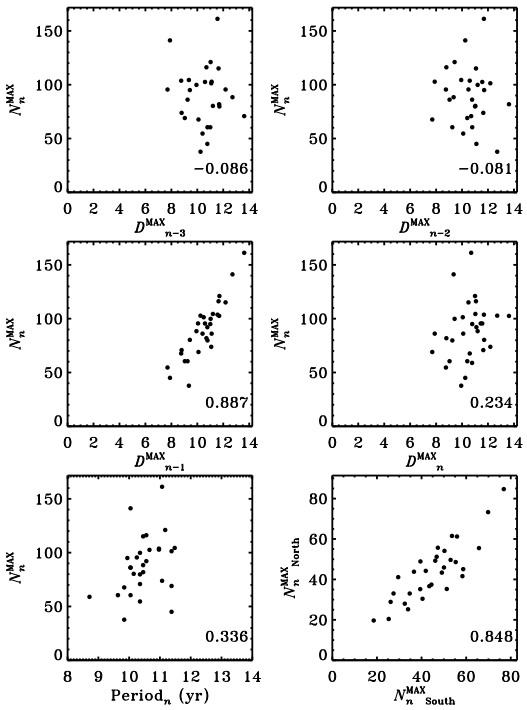

Figure 6. Amplitude (maximum pseudo-SSN) of cycle n as a function of maximum axial dipole moment at the end of cycle $n-3$ (top left panel), of cycle $n-2$ (top right panel), of cycle $n-1$ (middle left panel), and of cycle n (middle right panel), for the 32-[half-]cycles run presented in Figure 5. Bottom left panel: cycle amplitude as compared to the period of the same cycle. Bottom right panel: cycle amplitude calculated independently in each hemisphere and plotted against one another. In each panel is also given the corresponding Pearson's linear coefficient.

Also shown in the bottom left panel of Figure 6 is an absence of net correlation between cycle amplitude and period. This slightly differs from a solar behavior as observations show that strong cycles are generally shorter than weak ones. Finally, the bottom right panel illustrates how the two hemisphere are correlated in terms of cycle amplitude.

4.3. *Long Term Variability*

Figure 7 illustrates the Fourier transform of the energy and "signed" pseudo-SSN temporal evolutions, averaged over ten independent realizations of a $\simeq$ 96-[half]-cycles tilt-quenched 2 × 2D dynamo, similar to the preceding $\simeq$ 32-[half]-cycles reference solution. The top two panels, obtained in the fully stochastic regime, show more variability than the bottom panels for which the simula-

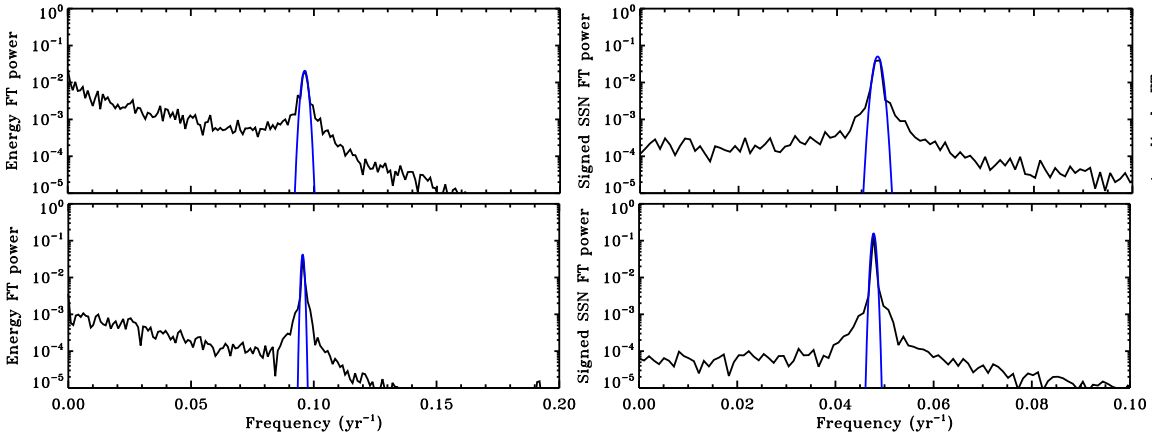

Figure 7. Fourier transforms of (left panels) the magnetic energy and (right panels) "signed" pseudo-SSN temporal evolution, averaged over ten independent realizations of a $\simeq$ 96-[half-]cycles tilt-quenched 2×2D dynamo simulation, in the fully stochastic (top panels) and partially stochastic (bottom panels) regime. Continuous blue curves illustrate the gaussian best fit to each spectrum.

tions were run with only part of the stochastic emergence processes. Both in the energy and pseudo-SSN temporal Fourier transforms, the width of the best-fit Gaussian in the fully stochastic case is about twice that in the partially stochastic one. The full magnetic cycle period, as revealed by the signed pseudo-SSN temporal spectrum, peaks at a period of 20.8 ± 0.6 years (at the two sigma level) in the fully stochastic case and 20.9 ± 0.3 years in the partially stochastic case. The half-cycle period revealed by the oscillating magnetic energy peaks at 10.4 ± 0.2 years in the first case and 10.5 ± 0.1 years in the second one. These results indicate that despite the strong variability in cycle amplitude obtained in the simulations, the period is very robust, more than in the real Sun, even with the fully stochastic emergence procedure. The low-frequency ends of the spectra are also of interest, nearly an order of magnitude stronger in the fully stochastic case, for both the energy and the pseudo-SSN. In the fully stochastic case, the low-frequencies of the temporal spectrum for the energy harbor amplitudes comparable with the main oscillation amplitude, which confirm the long term memory embedded in the deep-seated magnetic structures. The effect is much less apparent at the surface as revealed by the temporal spectrum of the pseudo-SSN.

Figure 8 shows three different realizations, at the same dynamo number and quenching B_q...

From a set of 30 realizations similar to the preceding ones, three die before reaching the 32th cycle and seven before reaching the 96th cycle. The probability of a dynamo to remain active after a certain number of cycles thus decreases with time in a manner that could be compatible with a stochastically-driven asymptotic tendency. Simulation of tens of independent realizations over thousands of cycles would be required to evaluate the actual shape of this decreasing curve.

5. DISCUSSION

The dynamo solutions presented above result from the use of a model calibrated to cycle 21 emergence data through an optimization process operating on a specific goodness-of-fit measure and in a bounded search space. These bounds were set (loosely) on observational and/or physical grounds, but obviouly pose a restriction on the range of solutions accessible to the optimization. Could we do do better than the optimal solution listed in Table 1? We have carried out a number of alternate optimization runs in order to answer this question, as described in what follows.

An 18-parameter optimization similar that described in §**??** but using much broader ranges of parameter does manage to return a best-fit solution with $C = 0.97$, significantly better than the original 18-parameter best-fit solution, which has $C = 0.95$. This nominally superior fit, however, is achieved through of a low-latitude cut-off for the emergence function, down to $\ell^* = 30°$, which is clearly incompatible with instability diagrams for thin toroidal flux ropes.

We also carried out optimization runs in which the parameters defining the latitudinal dependence of the meridional flow (via Equations (**??**)—(**??**) are constrained to a narrower range of acceptable values, corresponding to the best-fit surface flux transport solution obtained in paper I. The best-fit solution from such an optimization reach only $C \simeq 0.86$; while the best-fit measures used in paper I is not the same as here, this is a significant difference. More worrisome is the fact that the surface meridional flow for the best-fit solution of Table 1, plotted on Figure 9, provides a rather poor fit to the Doppler observations of Ulrich (2010), which at low latitudes lie outside the range of acceptable solutions from the optimizatin run. The best-fit profile of paper I did much better in this respect (its range of acceptable solution indicated by the two dotted lines on Figure 9).

This suggests some incompatibility between the optimization of the SFT model relative to surface magnetograms and the optimization of the coupled SFT–FTD model relative to the shape of the butterfly diagram. The W21×8-11 optimal solution of §**??** still lies within the surface-optimized ranges for the maximum meridional flow amplitude u_0, the surface diffusivity η_R, and the exponential decay time τ_R, while the parameters q, v and w (see Equation (**??**)), setting the latitudinal dependence of the stream function, do not. Interestingly, despite significant variations in latitudinal profiles all acceptable solutions ($C \geq 0.9$) have a peak equatorward meridional flow speed of m s^{-1} near the base of the circulation cell; this is consistent with the deep meridional flow setting

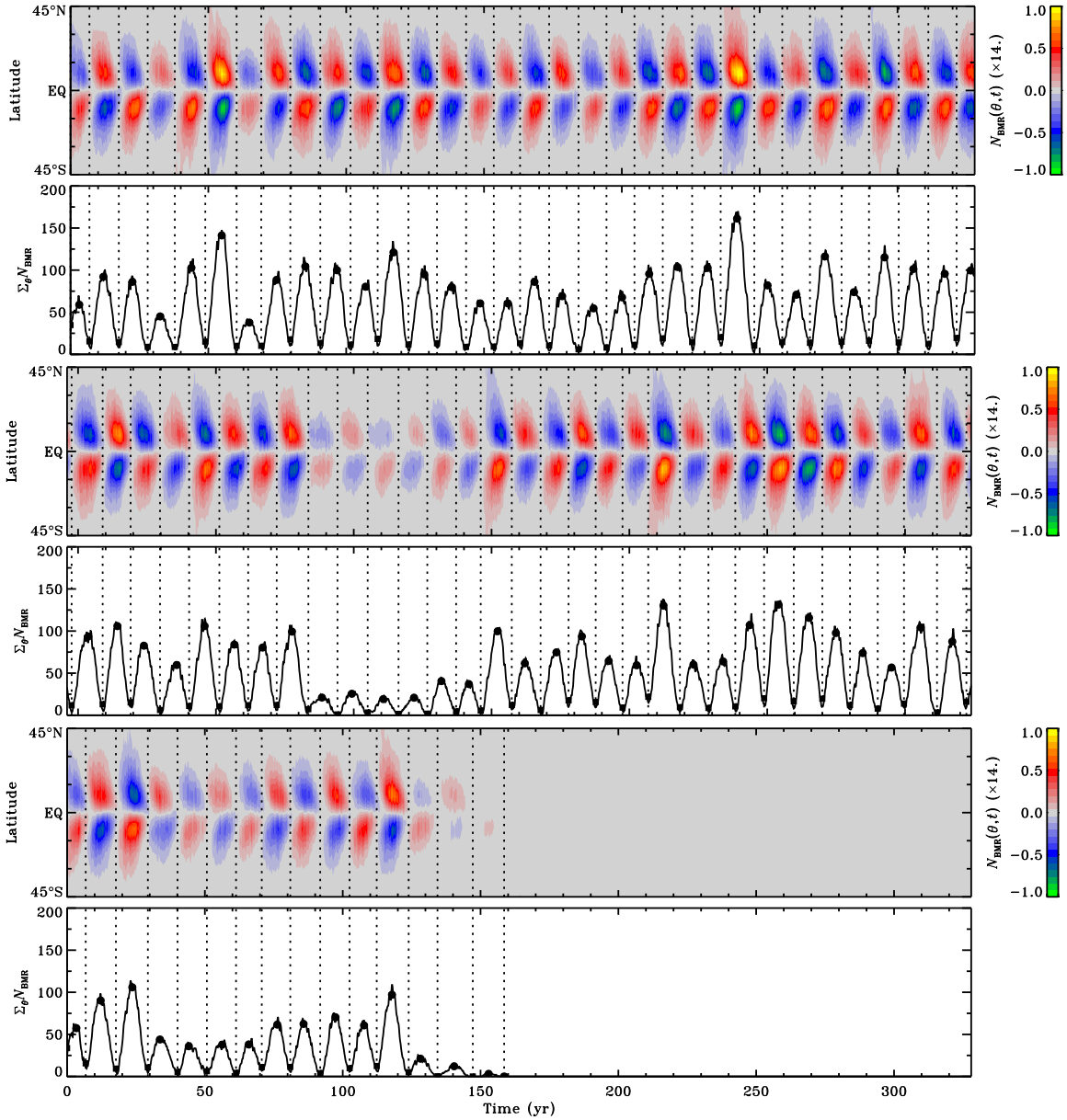

Figure 8. Time–latitude density plot (butterfly diagram) and corresponding monthly number (pseudo-SSN) of newly emerged BMRs, for our reference dynamo solution (same as middle panels of Figure 5) and two other realizations of a $\simeq$ 32-[half-]cycles tilt-quenched 2 × 2D dynamo simulation.

the cycle period in these models, which leads to a very tight constraint when fitting the butterfly diagram.

The analytic form adopted here for the meridional flow stream function is of course extremely simple: steady and separable in r and θ, which enforces the same latitudunal dependence at all depths, here defining a single flow cell per meridional quadrant. What our butterfly diagram-based goodness-of-fit measure thus constrains is primarily the flow at the base of the convection zone. The misfit with the results from purely surface optimization suggests that the internal flow is more complex than the single-cell profile used here. Indeed, the recent helioseismic inversions of Zhao et al. and Schad et al. (2013) suggest multiple cells in radius, which is known to have a large impact on the operation fo flux transport dynamos (e.g., Jouve & Brun 2007). The dynamo modelling work of Hazra et al. (2014) indicates, however, that provided additional transport processes such as turbulent diffusion and/or pumping can couple the surface and base of the convection zone, solar-like butterfly diagrams can be produced (see also Jiang et al. 2013).

Another physical inconsistency of the W21×8-11 optimal solution is the meridional flow's deep penetration below the base of the convection zone. This is known to be conducive to the production of solar-like butterfly diagrams (e.g., Nandy & Choudhuri 2002), but unlikely on dynamical grounds (Gilman & Miesch 2004), and delicate to reconcile with observed solar light element abundances (Charbonneau 2007). Finally, both observations (Ulrich 2010) and numerical simulations (Passos et al. 2012) suggest that the meridional flow may undergo systematic temporal variations in the course of the cycle,

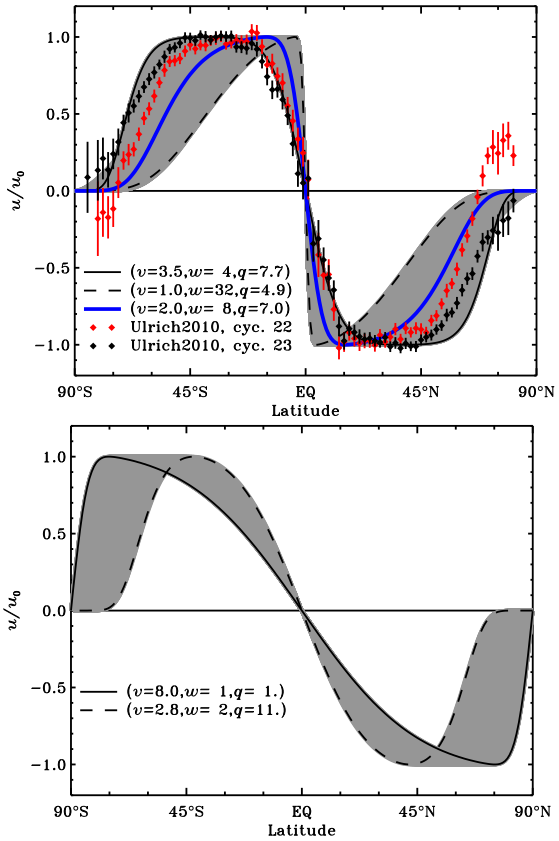

Figure 9. Observed and modeled latitudinal profiles of surface meridional flow. The gray band indicates the range of acceptable profiles in the W21-11 optimal solution of §**??**, while the two dotted line indicate the acceptable range obtained in paper I by fitting synoptic magnetograms. The solid dots are the Doppler measurements of Ulrich (2010) for cycles 22 and 23.

presumably driven by the cycling magnetic field. Such effects are *a priori* excluded from the meridional flow parametrization used here.

All these incompatibilities and inconsistencies most likely reflect, at least in part, the specific choices made for the parametrization of the meridional flow profile. An interesting possibility would be to use our genetic algorithm-based fitting technique to invert a spatially-resolved discretisation the internal meridional flow from the sunspot butterfly diagram. Such a method, dubbed genetic forward modelling, has already been used successfully to infer the rotational profile of the deep solar core from low-ℓ rotational frequency splittings (see Charbonneau et al. 1998).

Genetic forward modelling could also be used to invert stability diagrams for the emergence of BMRs. Our best-fit emergence function has $a = 0$ in Equation (**??**), implying that the emergence probability is primarily set by the strength of the toroidal magnetic component, in agreement with the idea that sunspots form from axisymmetric toroidal magnetic flux ropes located at of near the base of the convection zone. However, our eruption threshold of 200 Gauss is rather low, even if some level of amplification is expected in forming a compact flux rope from a diffuse magnetic field. There is clearly room for improvement in this model component.

Additional refs:

Charbonneau, P., Tomczyk, S., Schou, J., Thompson, M.J. 1998, ApJ, 496, 1015

Charbonneau, P. 2007, AdvSpRes, 39, 1661

Gilman, P.A., & Miesch, M.S. 2004, ApJ, 611, 568

Hazra, G., Karak, B.B., Choudhuri, A.R. 2014, ApJ, 782, 93

Jiang, J., Cameron, R.H., Schmitt, D., & Isik, E. 2013, A&A, 553, 128

Jouve, L., & Brun, A.S. 2007, A&A, 474, 238

Nandy, D., & Choudhuri, A.R. 2002, Sci, 296, 1671

Passos, D., Charbonneau, P., & Beaudoin, P. 2012, SolP, 279, 1

Schad, A., Timmer, J., & Roth, M. 2013, ApJL 778, L38

Zhao, J., Bogart, R.S., Kosovichev, A.G., Duvall, T.L.Jr., & Hartlep, T., 2013 ApJL 774, L29

Model uses single-cell meridional flow; recent helioseismic inversions suggest more complicated pattern. Best-fit model requires latitudinal profile differing from those obtained in paper I by fitting synoptic magnetograms only with surface flux transport model (FIG: and explain more).

Other potentially non-solar-like feature: deply penetrating meridional flow.

These problems are not critical, as they arise primarily from specific choices made for the analytical functional form adopted to describe the meridional flow. Confident that these models ingredients can be modified to yield comparably good (and perhaps better) representations of the solar cycle, while remaining in better agreement with helioseismic inferences regarding flos in the solar interior. A GA-based inversion of the internal meridional flow profile based on matching synoptic magnetograms and constrained by surface flow measurements could even be contemplated.

[Recall the parameters optimal values...]

[What happens if we change those values...]

[What is the physical meaning of the optimal solutions...]

[How does it compare with preceding models...]

[Low amplitude for Bphi...]

[Does the τ corresponds to analysis by Baumann2006 ? $\tau \sim 5$ years corresponds to decay of dipole mode ($n = 0, l = 1$) for volume diffusion coefficient of 100 km^2 s^{-1}, which corresponds to values obtained for the turbulent diffusivity in the convection zone.]

...

6. CONCLUSIONS

In this paper we have described a new solar cycle model based on the BL mechanism of poloidal field regeneration through the surface decay of active regions. This new model is based on the coupling of a conventional latitude–longitude simulation of surface magnetic flux evolution (as described in Paper I), coupled to an equally conventional axisymmetric kinematic flux transport dynamo model defined in a meridional plane (closely following Charbonneau et al. 2005). The novelty lies in the coupling between these to model components: the sur-

face flux evolution simulation provides the source term of the internal dynamo through the surface boundary condition; while the internal dynamo provides the magnetic flux emergence, in the form of pseudo-sunspot bipolar pairs, that act as a source in the surface magnetic flux simulation. The properties of these synthetic bipolar pairs —flux distribution, component separation, tilt angles, etc— are tailored to reflect observed statistical properties of real sunspots and active regions, as documented in Paper I (Appendix).

The other key aspect of the coupling is the emergence function, which controls the probability of bipole emergence as a function of the spatiotemporal distribution of the deep-seated magnetic field produced by the dynamo component of the coupled model. The emergence probability is assumed to scale linearly with this emergence function, with the proportionality constant acting as the dynamo number for the full coupled model.

The coupled model involves a number of parameters and functionals that cannot be set from first principle, and thus must be optimized to provide the best possible fit to solar observations. We opted to carry out this optimization task through a GA-based maximization of the fit between the spatiotemporal distribution of sunspot emergences (butterfly diagram) as produced by the model, and the cycle 21 emergence data of Wang & Sheeley (1989). This scheme returns not only a globally optimal solution, but also Monte Carlo-like error estimates on best-fit parameters values.

The magnetic cycles generated by this dynamo model are intrinsically non-steady, due primarily to the large statistical scatter about the mean East–West tilt pattern of BMRs (as embodied in Joy's Law). This is expected, since the axial dipole component of the bipolar pair is determined by this tilt. As a consequence, a critical dynamo number can only be defined in a statistical sense.

Even though the amplitude of successive simulated cycles are strongly affected by the specific stochastic realization of flux, separation and tilts in the course of a given cycle, even in the linear regime the cycle period is largely insensitive to the value of the dynamo number. A quenching parametrization of the mean tilt angle based on the strength of the internal magnetic field readily stabilize the mean cycle amplitude, but large fluctuation about this mean nonetheless persist. Such a quenching is supported by both observational analyses (see Dasi-Espuig et al. 2010 *Alex:* [correlations =¿ lien amplitude cycle vs tilt, mais pas directement]) and modeling of the buoyant rise of thin magnetic flux tubes (see Fan 2009, § 5.1.2, and references therein).

One consequence of tilt quenching is that a very high amplitude cycle tend to be followed by a lower-than-average cycle. *Alex:* [Je ne dirais pas nécessairement ça... Un cycle de forte amplitude est aussi simplement difficile à renverser, ce qui conduit naturellement à un cycle subséquent plus faible...] Very low amplitude cycles can also be produced by unfavorable emergence patterns, which then lead to persistently low amplitudes in subsequent cycles, with slow recovery to normal amplitude values. Despite these strong fluctuations in cycle amplitudes, the magnetic cycle is characterized by good hemispheric coupling, in terms of both hemispheric cycle amplitude and timing of hemispheric minima/maxima.

As a descriptive representation of the observed solar cycle, the model reproduces a number of well-known features. The dipole peaks at or slightly before the time of pseudo-sunspot cycle minimum, and its amplitude shows no correlation with the maximum (synthetic) [pseudo]-sunspot number of the ending cycle. This is a direct consequence of the strong stochasticity introduced by the realization of tilt patterns throughout the cycle, which is the primary source of cycle amplitude fluctuations. However, the model reproduces the observed positive correlation between dipole strength at cycle minimum and the amplitude of the subsequent pseudo-sunspot cycle. This indicates that, as in the real Sun, the dipole moment generated in the model is a good precursor of cycle amplitude.

Room for improvement certainly remains. The model fails to reproduce the observed moderate anticorrelation between cycle amplitude and duration, producing instead a very weak positive correlation between these two quantities. While a few extant kinematic flux transport dynamo models do better in this respect (e.g., Karak & Choudhuri 2011) *Alex:* ['The Waldmeier effect and the flux transport solar dynamo'], another possibility is that the origin of this pattern is to be found in dynamical effects, namely the magnetic backreaction on large-scale flows. The recent analyses of Passos et al. (2012) suggest that an increase in the speed of the deep equatorward meridional flow may indeed be driven by a higher-than-average large-scale magnetic field, which in advection-dominated flux transport dynamos would be expected to lead to a proportional reduction in cycle period (see, e.g., Dikpati & Charbonneau 1999).

The long timescale behavior of the simulated cycles also shows some interesting features, some solar-like and others less so. The model autonomously generates significant power at low frequencies, but without any well-defined spectral peaks that could be associated with Gleissberg-like long periodicities. The model does produce occasional Dalton-minimum-like periods of successive low amplitude cycles, and can also spontaneously shut down the cycle and enter a non-cycling grand-minima-like state, through an unfavorable stochastic pattern of bipolar pseudo-sunspot emergences in the course fo a cycle. This is a relatively common occurrence for a simulation using the best-fit parameter values obtained in § 3: about one fourth of simulations initialized with distinct random seeds were found to undergo shutdown at some point during a 100-cycle long time span.

In subsequent papers in this series we will investigate cycle fluctuation patterns in greater detail, and quantify the occurrence statistics of Dalton-like minima. The few such events found so far in our extant simulation runs suggest that entry into these failed minima is rapid, from one (half-)cycle to the next, while recovery to average cycle amplitudes is more gradual. We also plan to add a weak turbulent alpha-effect in the convective envelope portion of the domain, and investigate whether this can pull the model out of a shutdown state, as existing simulations have already suggested (e.g., Ossendrijver 2000; Karak & Choudhuri 2013; Hazra et al. 2014).

Because it includes an explicit, spatially-resolved representation of the solar "surface", the solar cycle model presented here is ideally suited for assimilation of magnetographic data. The resulting data-driven model could then be used to carry out prediction of upcoming cy-

cles. The results presented in this paper indicate that an accurate determination of the tilt angles of individual emerging bipolar sunspot pairs will be a critical element of such an endeavor.

BMR bipolar magnetic region

BL Babcock–Leighton

FTD flux transport dynamo

GA genetic algorithm

MHD magnetohydrodynamics

SFT surface flux transport

We are grateful to some people.... Thanks to funding from FRQNT... Etc. LaTeX...

REFERENCES

Babcock, H. D. 1959, ApJ, 130, 364
Babcock, H. W. 1961, ApJ, 133, 572
Babcock, H. W., & Babcock, H. D. 1955, ApJ, 121, 349
Baumann, I., Schmitt, D., & Schüssler, M. 2006, A&A, 446, 307
Baumann, I., Schmitt, D., Schüssler, M., & Solanki, S. K. 2004, A&A, 426, 1075
Burnett, D. S. 1987, Finite element analysis: From concepts to applications (Reading, Massachusetts: Addison-Wesley Pub. Co.)
Charbonneau, P. 2002, NCAR Technical Note, NCAR/TN-451+STR, 1
Charbonneau, P. 2010, Living Reviews in Solar Physics, 7, 3
—. 2014, ARA&A, 52, 251
Charbonneau, P., Christensen-Dalsgaard, J., Henning, R., et al. 1999, ApJ, 527, 445
Charbonneau, P., & Knapp, B. 1995, NCAR Technical Note, NCAR/TN-418+IA, 1
Charbonneau, P., St-Jean, C., & Zacharias, P. 2005, ApJ, 619, 613
Choudhuri, A. R., Chatterjee, P., & Jiang, J. 2007, Physical Review Letters, 98, 131103
Choudhuri, A. R., Schussler, M., & Dikpati, M. 1995, A&A, 303, L29+
Dasi-Espuig, M., Solanki, S. K., Krivova, N. A., Cameron, R., & Peñuela, T. 2010, A&A, 518, A7
Dikpati, M. 2011, ApJ, 733, 90
Dikpati, M., & Charbonneau, P. 1999, ApJ, 518, 508
Dikpati, M., de Toma, G., & Gilman, P. A. 2006, Geophys. Res. Lett., 33, 5102
Dikpati, M., & Gilman, P. A. 2001, ApJ, 559, 428
—. 2007, Sol. Phys., 241, 1
Durney, B. R. 1995, Sol. Phys., 160, 213
Fan, Y. 2009, Living Reviews in Solar Physics, 6, 4
Ferriz-Mas, A., Schmitt, D., & Schuessler, M. 1994, A&A, 289, 949
Hale, G. E., Ellerman, F., Nicholson, S. B., & Joy, A. H. 1919, ApJ, 49, 153
Hazra, S., Passos, D., & Nandy, D. 2014, ApJ, 789, 5
Howard, R. F. 1991, Sol. Phys., 136, 251
Karak, B. B., & Choudhuri, A. R. 2011, MNRAS, 410, 1503
—. 2013, Research in Astronomy and Astrophysics, 13, 1339
Karak, B. B., Jiang, J., Miesch, M. S., Charbonneau, P., & Choudhuri, A. R. 2014, Space Sci. Rev., 186, 561
Leighton, R. B. 1964, ApJ, 140, 1547
Lemerle, A., Charbonneau, P., & Carignan-Dugas, A. 2015, ApJ, 810, 78
Metcalfe, T. S., & Charbonneau, P. 2003, Journal of Computational Physics, 185, 176
Miesch, M. S., & Dikpati, M. 2014, ApJ, 785, L8
Muñoz-Jaramillo, A., Dasi-Espuig, M., Balmaceda, L. A., & DeLuca, E. E. 2013, ApJ, 767, L25
Muñoz-Jaramillo, A., Nandy, D., Martens, P. C. H., & Yeates, A. R. 2010, ApJ, 720, L20
Nandy, D., & Choudhuri, A. R. 2001, ApJ, 551, 576
Nelson, N. J., Brown, B. P., Brun, A. S., Miesch, M. S., & Toomre, J. 2013, ApJ, 762, 73
Nelson, N. J., Brown, B. P., Sacha Brun, A., Miesch, M. S., & Toomre, J. 2014, Sol. Phys., 289, 441
Ossendrijver, M. A. J. H. 2000, A&A, 359, 1205
Parker, E. N. 1955, ApJ, 122, 293
Passos, D., & Charbonneau, P. 2014, A&A, 568, A113
Passos, D., Charbonneau, P., & Beaudoin, P. 2012, Sol. Phys., 279, 1
Schmitt, D. 1987, A&A, 174, 281
Schrijver, C. J. 2001, ApJ, 547, 475
Schrijver, C. J., De Rosa, M. L., & Title, A. M. 2002, ApJ, 577, 1006
Schussler, M., Caligari, P., Ferriz-Mas, A., & Moreno-Insertis, F. 1994, A&A, 281, L69
Snodgrass, H. B. 1983, ApJ, 270, 288
Ulrich, R. K. 2010, ApJ, 725, 658
van Ballegooijen, A. A., & Choudhuri, A. R. 1988, ApJ, 333, 965
Wang, Y.-M., Lean, J., & Sheeley, Jr., N. R. 2002a, ApJ, 577, L53
Wang, Y.-M., Nash, A. G., & Sheeley, Jr., N. R. 1989, Science, 245, 712
Wang, Y.-M., & Sheeley, Jr., N. R. 1989, Sol. Phys., 124, 81
—. 1991, ApJ, 375, 761
Wang, Y.-M., Sheeley, Jr., N. R., & Lean, J. 2002b, ApJ, 580, 1188
Weber, M. A., Fan, Y., & Miesch, M. S. 2011, ApJ, 741, 11
Yeates, A. R., & Muñoz-Jaramillo, A. 2013, MNRAS, 436, 3366